ABSTRACT

Title of dissertation: Measuring topology of BECs
in a synthetic dimensions lattice

Dina Genkina
Doctor of Philosophy, 2018

Dissertation directed by: Professor Ian Spielman
Department of Physics

Measuring topology of BECs in a synthetic dimensions lattice

by

Dina Genkina

Dissertation submitted to the Faculty of the Graduate School of the
University of Maryland, College Park in partial fulfillment
of the requirements for the degree of
Doctor of Philosophy
2018

Advisory Committee:
Professor Ian Spielman, Chair/Advisor

Chapter 2:   Atom Light Interactions

2.1   Near-resonant atom-light interaction

In this section, we will assume the atom can be treated as a two-level system: one with a ground and excited atomic state, with an energy difference of energy difference $\hbar\omega_0$. When such an atom, starting in the ground state, is illuminated by a laser beam with frequency $\hbar\omega_{\mathrm{L}}$, there are three kinds of transitions that occur: during aborption the atom aborbs a photon from the laser and goes from the ground to the excited state; during stimulated emission, the atom emits a photon into the field of the laser beam and jump from the excited to the ground state; during spontaneous emission, the atom decays to the ground state from the excited state with no help from the laser, emitting into a random vacuum mode. Stimulated emission results in coherent light co-propagating with the laser beam, while spontaneous emission results in light scattering incoherently in any direction. The rate of spontaneous emission from an excited state is given by the natural transition linewidth of the transition Γ.

On timescales short compared to $1/\Gamma$, spontaneous emission can be ignored, and an atom undergoes coherent Rabi oscillations between the ground and excited states via cycles of absorption and stimulated emission [1]. Taking c_g and c_e to be the time-dependent coefficients multiplying the eigenstate wavefuntions of the ground and excited state respectively, and assuming the atom starts in the ground

state $c_g(t = 0) = 1$, the excited state population is given by

$$c_e(t) = -i\frac{\Omega}{\Omega'}\sin\left(\frac{\Omega' t}{2}\right)e^{-i\delta t/2}, \tag{2.1}$$

where Ω is the Rabi frequency given by $\Omega^2 = \frac{\Gamma\lambda_L^3}{h(2\pi)^3}I$, with λ_L as the laser wavelength, h as Plank's constant and I as the laser intensity, $\Omega' = \sqrt{\Omega^2 + \delta^2}$ is the generalized Rabi frequency and $\delta = \omega_0 - \omega_\mathrm{L}$ is the detuniong of the laser from atomic resonance.

In the regime where spontaneous emission cannot be ignored, Rabi oscillations of each individual atom are intermittently interrupted by decay to the ground state. Averaging over an atomic ensamble, on the time scale of a single Rabi oscillation the overall excited state population reaches a steady state, and the rate of spontaneous emission becomes constant. Since during spontaneous emission the ejected photon can go into any vacuum mode, this process can be thought of as the scattering of photons by the atoms. This scattering rate is given by [1]

$$\gamma_\mathrm{sc} = \frac{\Gamma}{2}\frac{I/I_\mathrm{sat}}{1 + 4(\delta/\Gamma)^2 + I/I_\mathrm{sat}}, \tag{2.2}$$

where I_sat is the saturation intensity. This is the intensity at which the timescale of spontaneous emission matches the Rabi oscillation rate, reducing the capacity for absorption of extra light.

2.2   Absorption imaging

Absorption imaging takes advantage of the on-resonant interaction described in the previous section. An on or near-resonant laser beam ($\delta/\Gamma \ll 1$) is shined at the atoms, and the aborbed light acts to create a shadow in the shape of the atoms in the laser beam. This beam with the shadow is then imaged on a camera, in our case a CCD, as depicted in Figure 1a (top). This is called the atom image,
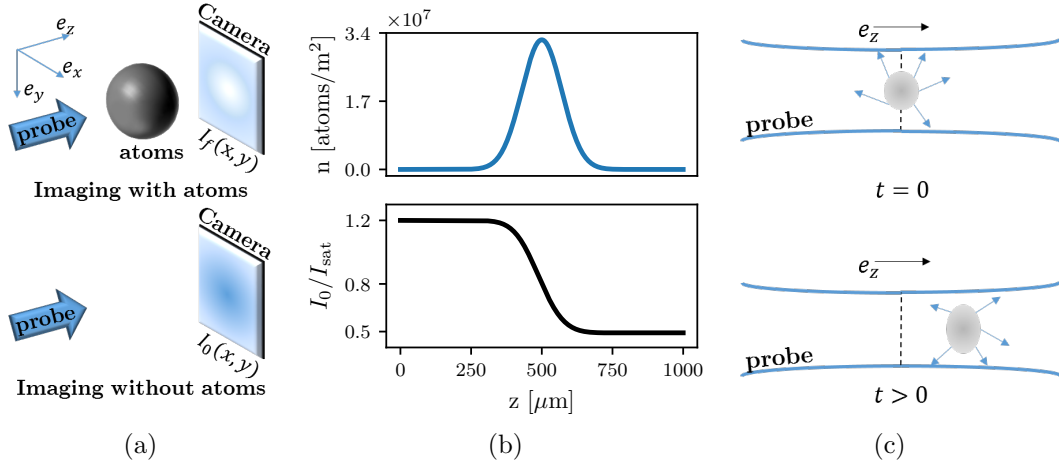
Figure 1: Absorption imaging. (a) Near resonant probe light illuminates the atoms, and the transmitted light (containing a shadow of the atoms) is imaged on the camera. A second image taken with no atoms provides a reference. (b) The probe beam is partially absorbed as it traverses the cloud, and the intensity seen by atoms further along the imaging direction $e_{\mathbf{z}}$ is lowered. (c) An atomic cloud illuminated by a probe light field absorbs photons from the probe and re-emits them in all directions. This process results in a net acceleration of the cloud in the direction of the probe light as well as diffusive spreading in the transverse directions.

and the intensity distribution over the camera is denoted by $I_f(x, y)$, where the subscript f stands for final - the intensity after the light has encountered the atoms. To quantify the 'shadowed out' intensity, after the atoms have left the trap the same laser intensity is shined directly at the camera, as in Figure 1a (bottom). This is called the probe image, and the intensity distribution over the camera is denoted by $I_0(x, y)$, where the subscript 0 indicated initial - the intensity before the light had encountered the atoms.

To recover the atom number distribution encountered by the light, consider an atomic cloud with 3D density $\rho(x, y, z)$. Since we can only obtain 2D information from the camera, we can only hope to recover a 2D atomic column density $n(x, y) = \int \rho(x, y, z) \mathrm{d}z$. Focusing in on a single pixel of the camera, we can consider a single value of I_0 and I_f to recover a local n. As the laser light propagates through the atomic cloud, the intensity of the light will diminish due to absorption. This

absorption as a function of propagation direction z can be expressed using the scattering rate equation Eq. 2.2 as the number of photons scattered by the atoms (proportional to the atomic density times the scattering rate) times the photon energy $\hbar\omega_{\mathrm{L}}$:

$$\frac{d}{dz}\frac{I(z)}{I_{\mathrm{sat}}} = -\hbar\omega_{\mathrm{L}}\rho(z)\gamma_{sc}(z) = -\rho(z)\sigma_0\frac{I(z)/I_{\mathrm{sat}}}{1+4\delta^2/\Gamma^2+I(z)/I_{\mathrm{sat}}}, \qquad (2.3)$$

where the resonant scattering cross section is $\sigma_0 = 3\lambda_0^2/2\pi$, and λ_0 is the wavelength asociatted with atomic resonance.

Integrating both sides of Eq. 2.3, we obtain

$$\sigma_0 n = \left(1+4\delta^2/\Gamma^2\right)\ln(I_0/I_f) + (I_0 - I_f)/I_{\mathrm{sat}}. \qquad (2.4)$$

The quantity $OD = ln(I_0/I_f)$ is called the optical depth of the cloud. When the probe intensity I_0 is much smaller than the saturation intensity, the second term in Eq. 2.4 becomes negligible. Assuming further that the probe light is on resonance, $\delta = 0$, the atomic column density becomes simply $\sigma_0 n = OD$. Figure 1b shows a Gaussian atomic density distribution (top) and the resulting probe intensity as a function of position in the cloud (bottom). The intensity drops from its initial to final value gradually as it traverses the cloud.

However, there is an important effect that the above equations do not account for. Namely, as the atoms absorb light from the probe beam, they also get a momentum kick equal to the momentum of a photon during each collision $\hbar k_r = h/\lambda_L$ in the direction of propagation. It is true that the absorbed photon will then be re-emitted by the atom, inducing a loss of momentum, but since this happens through the process of spontaneous emission into a random vacuum mode, the average momentum kick acquired this way over many re-emissions will average to zero. On average, each photon absorbed will induce a change in velocity of the atom of $v_r = \hbar k_r/m$,

where m is the atomic mass, as depicted in Fig. 1c. As the velocity of the atom changes, due to the Doppler effect, the apparent laser frequency will change as well. Therefore, even if the laser light is exactly on-resonant for a stationary atom, it will become off-resonant for longer imaging times, and Eq. 2.3 will acquire a time dependence. For most experiments, this effect is small and can be neglected. However, if the imaging time becomes of order a recoil time t_r, a time after which the recoil-induced detuning δ becomes of order Γ, this effect becomes significant. We explore this effect in Chapter 3.

2.3 One dimensional optical lattices

2.3.1 Far off-resonant atom-light interaction

As described in section 2.1, on timescales where spontaneous emission can be neglected, two-level atoms exposed to laser radiation undergo coherent Rabi oscillations between the two levels. Starting with c_g and c_e as the time-dependent coefficients multiplying the eigenstate wavefuntions of the ground and excited state respectively, and assuming the atom starts in the ground state $c_g(t = 0) = 1$, we make the traditional transformation to the rotating frame:

$$c'_g(t) = c_g(t) \tag{2.5}$$

$$c'_e(t) = c_e(t)e^{-i\delta t}, \tag{2.6}$$

where δ is the detuning of laser light from resonance. In this frame, we can write the atom-light Hamiltonian in the $\begin{pmatrix} c'_g \\ c'_e \end{pmatrix}$ basis as:

$$H = \hbar \begin{pmatrix} -\delta/2 & \Omega/2 \\ \Omega/2 & \delta/2 \end{pmatrix}, \tag{2.7}$$

where Ω is the coupling strength, also known as the Rabi frequency. In the limit of no coupling, $\Omega = 0$, in the rotating frame the eigenenegies are $E_\pm = \pm\hbar\delta/2$. For non-zero coupling, finding the eigenvalues of H gives $E_\pm = \pm\hbar\sqrt{\delta^2 + \Omega^2}/2$. Therefore, the bare (without light) eigenenrgies are shifted in the presence of the light.

For a far detuned laser beam, one expects that no absorption of the light will actually take place, and the atom will remain entirely in the ground state. Indeed, solving the Shroedinger equation with the above Hamiltonian

$$i\hbar\frac{d}{dt}\begin{pmatrix} c'_g \\ c'_e \end{pmatrix} = H\begin{pmatrix} c'_g \\ c'_e \end{pmatrix} \tag{2.8}$$

we obtain the oscillating excited state population

$$c'_e(t) = -i\frac{\Omega}{\sqrt{\Omega^2 + \delta^2}}\sin\left(\frac{\sqrt{\Omega^2 + \delta^2}t}{2}\right), \tag{2.9}$$

where the amplitude of the oscillation approches zero in the limit $\Omega \ll \delta$. Thus, the only effect of the light in this regime is to shift the eigenenergies of the ground and excited states. Expanding the energies in the small parameter Ω/δ, we obtain the shifted energies $E_\pm = \pm\hbar\sqrt{\delta^2 + \Omega^2}/2 \approx \pm(\delta/2 + \Omega^2/4\delta)$. The shift from bare energy levels is thus

$$\Delta E_\pm = \pm\Omega^2/4\delta. \tag{2.10}$$

This laser intensity dependent energy shift is called the AC Stark shift, and is the basis of most laser created potentials for cold atoms.

For the ground state, and a red detuned laser beam (where the laser frequency is lower than the resonant frequency), this creates energy minima in locations of maximal laser intensity. For the lattice described in this chapter, as well as for the trapping of our atoms in the final stages of cooling, we use high power (up to 10 W) lasers with wavelength $\lambda_L = 1064$ nm.

2.3.2 Lattice Hamiltonian

Our 1-D optical lattice is created by retro-reflecting the $\lambda_L = 1064$ nm laser, creating a standing wave of light. Via the AC Stark shift, this creates a periodic potential for the atoms of the form

$$V = V_0 \sin^2(k_L x), \tag{2.11}$$

where $k_L = 2\pi/\lambda_L$ is the wavenumber associated with the lattice recoil momentum. The time-independent Hamiltonian, for some eigenenergy E_n, will be given by

$$-\frac{\hbar^2}{2m}\frac{d^2}{dx^2}\Psi_n(x) + V_0\sin^2(k_L x)\Psi_n(x) = E_n\Psi_n(x). \tag{2.12}$$

Since the potential is spatially periodic, we can invoke Bloch's theorem [2]:

$$\Psi_{n,q} = e^{iqx}u_{n,q}(x), \tag{2.13}$$

where q is the crystal momentum restricted to $\pm\hbar k_L$, and $u_{n,q}(x)$ is the spatially varying part of the wavefunction. Plugging this in to the Hamiltonian, we obtain

$$-\frac{\hbar^2}{2m}\left(-q^2 + 2iq\frac{d}{dx} + \frac{d^2}{dx^2}\right)u_{n,q}(x) + V_0\sin^2(k_L x)u_{n,q}(x) = E_n u_{n,q}(x). \tag{2.14}$$

Expanding $u_{n,q}(x)$ in Fourier components commensurate with the lattice period of $2k_L$ as $u_{n,q}(x) = \sum_{j=-\inf}^{\inf} a_j e^{i2k_L jx}$, we obtain

$$\sum_j \left(\frac{\hbar^2}{2m}(q + 2k_L)^2 a_j + V_0 \sin^2(k_L x) a_j \right) e^{i2k_L jx} = E_n \sum_j a_j e^{i2k_L jx}. \qquad (2.15)$$

Re-writing $\sin^2(k_L x) = (e^{-2ik_L x} + e^{2ik_L x} - 2)/4$, multiplying both sides by $e^{i2k_L j'x}$ and invoking $\sum c_j e^{ik(j-j')} = \delta_{jj'}$, where $\delta_{jj'}$ is the Kroniker delta and c_j are appropriately normalized coefficients, we get for any value of the index j

$$\frac{\hbar^2}{2m}(q + 2k_L j)^2 a_j - \frac{V_0}{4}(a_{j+1} + a_{j-1}) = E_n a_j. \qquad (2.16)$$

This can be expressed in matrix form

$$H_L = \begin{pmatrix} \ddots & & & & & \\ & \frac{\hbar^2}{2m}(q + 4k_L)^2 & \frac{V_0}{4} & 0 & 0 & 0 \\ & \frac{V_0}{4} & \frac{\hbar^2}{2m}(q + 2k_L)^2 & \frac{V_0}{4} & 0 & 0 \\ & 0 & \frac{V_0}{4} & \frac{\hbar^2}{2m}q^2 & \frac{V_0}{4} & 0 \\ & 0 & 0 & \frac{V_0}{4} & \frac{\hbar^2}{2m}(q - 2k_L)^2 & \frac{V_0}{4} \\ & 0 & 0 & 0 & \frac{V_0}{4} & \frac{\hbar^2}{2m}(q - 4k_L)^2 \\ & & & & & \ddots \end{pmatrix},$$

$$(2.17)$$

in the basis of momentum orders $|k\rangle = e^{ikx}$ given by:

$$
\begin{pmatrix}
\vdots \\
|q + 4k_L\rangle \\
|q + 2k_L\rangle \\
|q\rangle \\
|q - 2k_L\rangle \\
|q - 4k_L\rangle \\
\vdots
\end{pmatrix}.
\tag{2.18}
$$

This matrix can be diagonalized for every value of the crystal momentum q, withthe resulting band structure shown in Figure 2. It is convenient to define the lattice recoil energy $E_L = \hbar^2 k_L^2 / 2m$. Then, we can re-write the Hamiltonian with V_0 in units of E_L and momenta q in units of k_L as

$$
H_L/E_L =
\begin{pmatrix}
\ddots & & & & & \\
& (q+4)^2 & \frac{V_0}{4} & 0 & 0 & 0 \\
& \frac{V_0}{4} & (q+2)^2 & \frac{V_0}{4} & 0 & 0 \\
& 0 & \frac{V_0}{4} & q^2 & \frac{V_0}{4} & 0 \\
& 0 & 0 & \frac{V_0}{4} & (q-2)^2 & \frac{V_0}{4} \\
& 0 & 0 & 0 & \frac{V_0}{4} & (q-4)^2 \\
& & & & & \ddots
\end{pmatrix}.
\tag{2.19}
$$

In any numerical simulation, the number of momentum orders that can be included is finite. We determine the value of the parameter $n = \max(|j|)$ as the lowest n at which the eigenvalues stop changing to machine precision from $n - 1$. The code for finding and plotting the eigenvalues and eigenvectors of the lattice hamiltonian is included in Appendix [MAKE APPENDIX WITH CODE?].
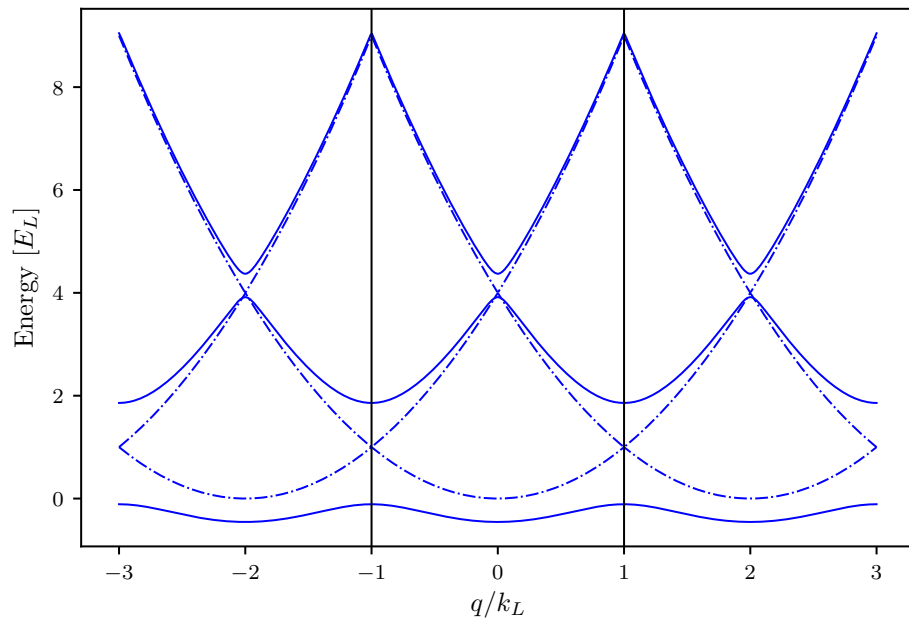
Figure 2: Lattice band structure in the extended zone scheme. The dashed lines represent the limit of zero lattice depth, with the regular parabolic dispersion relation of a free particle repating with reciprocal lattice period. The solid lines are the dispersion relation at $V_0 = 4.0E_L$, showing the opening of gaps at crossings of the zero lattice depth bands. The black lines demarcate the first Brillouin zone.

2.3.3 Tight binding approximation

In the limit of large lattice depths, $V_0 >\approx 5E_L$, the lattice Hamiltonian is well approximated by the tight-binding model. In the tight binding model, the basis is assumed to be a set of orthogonal functions, called Wannier functions, localized to each lattice site $|j\rangle$. The approximation lies in assuming only nearest neighbor tunnelings between the sites, forming the tight-binding Hamiltonian

$$H_\text{tb} = -t\,|j\rangle\,\langle j+1| + \text{H.c.}, \tag{2.20}$$

where t is the tunneling amplitude between nearest neighbor sites and H.c. stands for Hermitian conjugate. We have neglected the diagonal kinetic energy term, as it will be equal for every Wannier function $|j\rangle$ and thus represents a constant energy offset. All the information about the lattice depth is therefore reflected in the tunneling amplitude t.

The tight binding Hamiltonian can also be expressed in the momentum basis by Fourier transforming the basis functions:

$$|j\rangle = \frac{1}{\sqrt{N}} \sum_{k_j} e^{-ik_j j}\,|k_j\rangle, \tag{2.21}$$

giving the Hamiltonian

$$H_\text{tb} = -\frac{1}{N} \sum_{k_1} \sum k_2 t e^{-ijk_1} e^{ik_2(j+1)}\,|k_1\rangle\,\langle k_2| + \text{H.c} = 2t\cos(k)\,|k\rangle\,\langle k|. \tag{2.22}$$

From this we can directly read off the band structure of the tight binding Hamiltonian. First, we notice that we only obtain one band - to approximate higher bands with the tight binding approximation we would need to construct a different set of Wannier functions and a different tunneling strength. Second, we see that the lowest

band is simply a cosine - therefore we have solved for the band structure without even defining what the basis Wannier functions are! Third, the amplitude of the cosine function is given by the tunneling strength t. This gives us a good clue as to how to determine the appropriate tunneling given a lattice depth V_0 - simply find a t that matches the amplitude of the lowest band, which becomes cosinusoidal in the deep lattice limit.

The precise form of the Wannier functions depends on both the depth of the lattice and the band being reproduced. It is not necessary for us to find their full expression, as the band structure can be calculated without them. The definition, however, is

$$|j\rangle = \int_{\mathrm{BZ}} e^{i\phi(q)-iqja}\Psi_q(x)\mathrm{d}q, \tag{2.23}$$

where the integral is over the Brillouin zone, from $-k_L$ to k_L, a is the lattice spacing $\lambda_L/2$, and Ψ_q is the Bloch wavefunction at crystal momentum q, and $\phi(q)$ is the phase associated with each Bloch wavefuntion. The Bloch wavefunctions individually have arbitrary phase. The phase plays an important role in combining the Bloch wavefunctions into a Wannier function, finding the proper phase relationship to make the wavefunction maximally localized at each site [3].

2.3.4 Pulsing vs adiabatic loading of the lattice

The lattice depth parameter $V_0/4$, for a range of values, can be well calibrated experimentally by pulsing on the lattice. Here, the word pulsing indicates that the lattice is turned on fully non-adiabatically, if not instantaneously, such that the original bare momentum state is projected onto the lattice eigenbasis, as shown in Figure 5a. If the atoms start out stationary in the trap, the bare state in the

momentum basis is simply

$$|\Psi_0\rangle = \begin{pmatrix} \vdots \\ 0 \\ 0 \\ 1 \\ 0 \\ 0 \\ \vdots \end{pmatrix}, \tag{2.24}$$

as depicted in Figure 5b.

Since the lattice eigenbasis is distinct from the bare one, instiantaneously turning on the lattice will necessarily excite the atoms into a superposition of lattice eigenstates, each evolving with a different phase according to the eigenenergy while the lattice is on, as shown in Figure 5c. Then, when the lattice is snapped back off, the wavefunction is projected back into the bare basis, and the varying phase accumulation results in a beating of the different momentum orders, see Figure 5d. This can be calculated simply by using the time evolution operator

$$|\Psi(t)\rangle = e^{-iH_L t/\hbar} |\Psi_0\rangle. \tag{2.25}$$

By pulsing on the lattice for variable amounts of time t, we can obtain fractional populations in the different momentum states. Time-of-flight imaging captures the momentum distribution of the cloud, and the different entries of $\Psi(t)$ in the momentum basis will thus appear as different clouds on the absorption image, as shown in Figure 4a. The fractional population in these clouds corresponds to a measurement of $|a_j|^2$. Typically for our values of the lattice depth $V_0 < 10E_L$, it is sufficient to simply count three central momentum orders, $k = q, q \pm 2k_L$. Then, we can fit Eq. 2.25 to the data with fitting parameter V_0, thus deducing the lattuce depth. Some
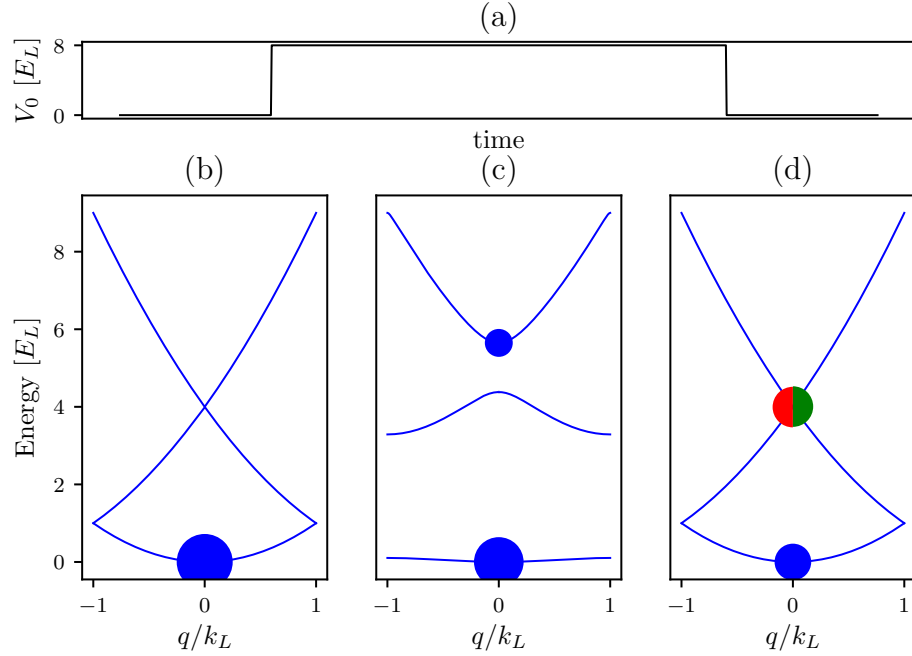
Figure 3: Lattice pulsing. (a) Lattice depth as a function of time during a pulsing experiment. The lattice is turned on instantaneously at $t = 0$ and held on for a variable amount of time until being turned off instantaneously at a final time $t = t_f$. (b) Atomic population before $t = 0$. The dispersion relation is that of a free particle, and all of the atoms start out at $q = 0$ in the lowest energy level. Here, the area of the dots is proportional to the fractional population in the energy state. (c) Atomic population after the lattice is turned on for a lattice depth of $V_0 = 8.0E_L$. The energy spectrum now shows the lattice band structure, and some atomic population is projected onto the excited bands. (d) Atomic population after the lattice is snapped off at $t_f = 150$ μs. The wavefunction is projected back onto the bare states, with some fraction (blue circle) in the lowest band at $k = 0$ and some fraction in the excited band, with equal population being projected onto the $k = 2k_L$ (green) and $k = -2k_L$ (red).
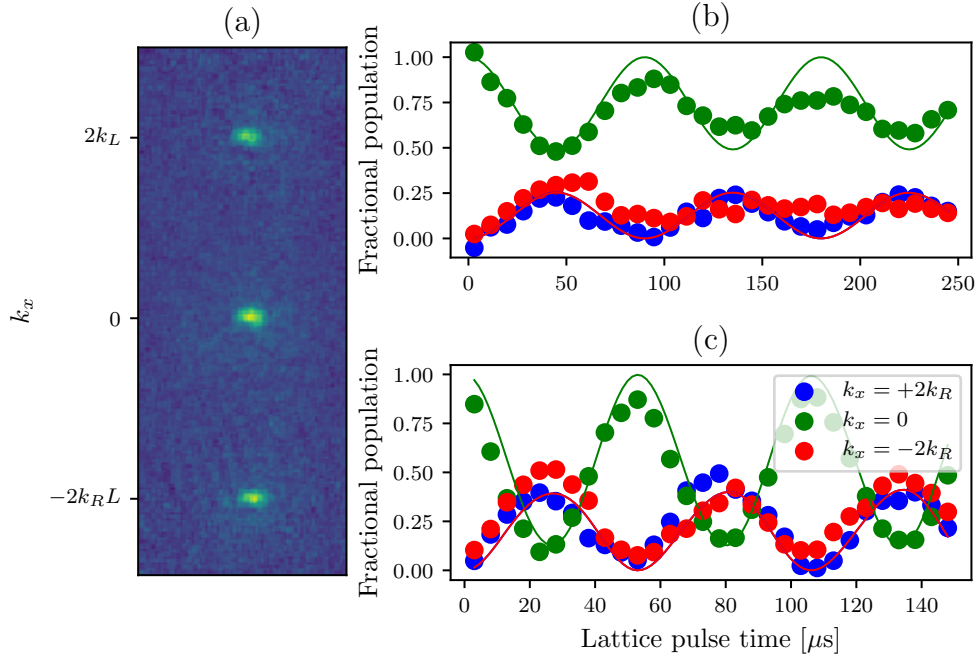
Figure 4: Lattice pulsing for calibration. (a) An example time-of-flight image from a pulsing experiment. The three different clouds are different momentum orders. (b) Fractional populations in the different momentum orders as a function of pulsing time at a low lattice power. Data is indicated by dots and best fit theory is represented by lines. The lattice depth from fit is $V_0 = 5.57 \pm 0.07 E_L$. (c)Fractional populations in the different momentum orders as a function of pulsing time at a higher lattice power. Data is indicated by dots and best fit theory is represented by lines. The lattice depth from fit is $V_0 = 12.69 \pm 0.07 E_L$.

examples of these pulsing experiments are presented in figure 4b,c.

In contrast to pulsing, adiabatic loading turns the lattice on slowly, such that the atomic wavefunction starting in the bare ground state can continuously adjust to remain in the ground state of the current Hamiltonian, without projecting onto any of the higher bands. This process is illustrated in Figure 5. The adiabatic timescale depends on the spacing between the ground and next excited band (or if starting in a different eigenstate, the nearest eigenstate). If the energy difference between the ground and first excited state is ΔE, the timescale on which the lattice is turned on must fullfill $t \gg h/\Delta E$.
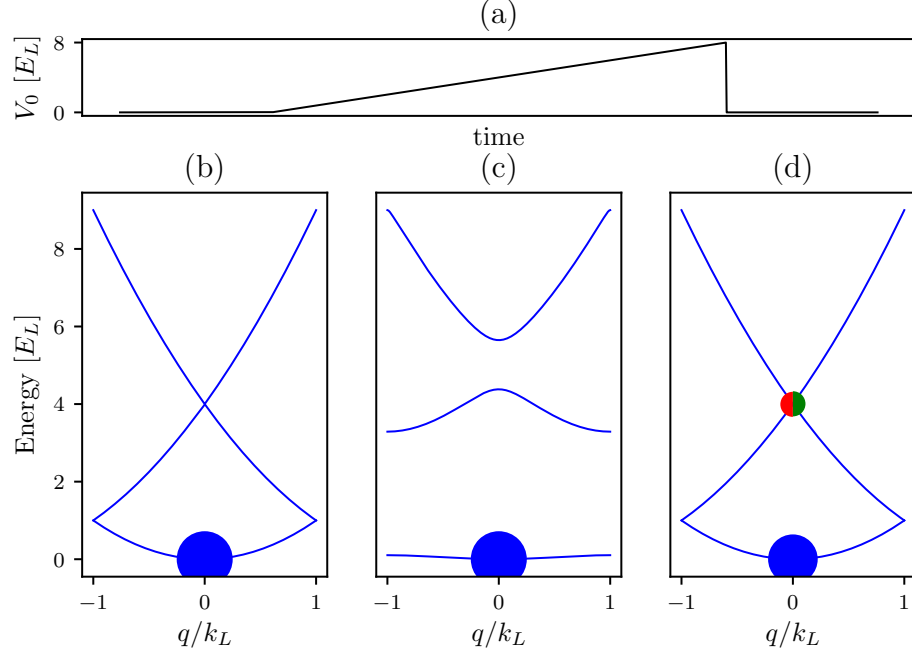
Figure 5: Adiabatic lattice loading. (a) Lattice depth as a function of time during adiabatic turn-on. The lattice is ramped on starting at $t = 0$, slowly increasng to a final lattice depth and turned off instantaneously at a final time $t = t_f$. (b) Atomic population before $t = 0$. All atoms are at $k = 0$ in the lowest bare band. (c) Atomic population after the lattice is turned on adiabatically to a lattice depth of $V_0 = 8.0E_L$. All atoms remain in the lowest band, but the band is no longer bare. (d) Atomic population after the lattice is snapped off. The wavefunction is projected back onto the bare states, with some fraction (blue circle) in the lowest band at $k = 0$ and some fraction in the excited band, with equal population being projected onto the $k = 2k_L$ (green) and $k = -2k_L$ (red). Since the lowest lattice band is a superposition of bare bands, some atoms are excited to the higher bare bands.

2.4   Raman and rf coupling

2.4.1   Hyperfine structure

Alkali atoms' energy levels can be understood as primarily the energy state of the single electron in the outer shell. Fine structure arises from different combinations of angular momenta, including orbital angular momentum of the outermost electron with respect to the nucleus $\mathbf{L}$, the electron spin $\mathbf{S}$ and the nuclear spin $\mathbf{I}$. The total electron angular momentum is the combination of orbital and the spin angular momenta $\mathbf{J} = \mathbf{L} + \mathbf{S}$, and the quantum number can be any integer $|L - S| \leq J \leq |L + S|$. The ground state of ^{87}Rb, in term notation $^{2S+1}L_J$ is $^2S_{1/2}$, where S is orbital notation indicating $L = 0$. Since the total spin quantum number $J = 1/2$, this produces two possible spin projection quantum numbers, $m_J = \pm 1/2$.

There is also a contribution from the nuclear spin $\mathbf{I}$, resolvable at low magnetic fields, which gives rise to hyperfine structure of the states. For ^{87}Rb, $I = 3/2$. The total spin, including nuclear spin, is indicated by the quantum number F, and $|J - I| \leq F \leq |J + I|$. The interaction with the nuclear spin splits the ground state of ^{87}Rb into two manifolds, $F = 1$ and $F = 2$, with three hyperfine states in the $F = 1$ manifold ($m_F = 0, \pm 1$) and five hyperfine states in the $F = 2$ manifold ($m_F = 0, \pm 1, \pm 2$). These states couple to an external magnetic field B_z along some direction $\mathbf{e}_z$ via the Hamiltonian $H_B = \mu_B(g_J J_z + g_I I_z)B_z/\hbar$. Here μ_B is the Bohr magneton, and g_J and g_I are Lande g-factors. Since $g_J \gg g_I$, at high fields the nuclear spin interaction becomes small compared to the total energy shift, and the levels are grouped according to their m_J quantum number, as seen in Figure 6.

At low fields, however, the states are approximately linearly dependent on the m_F quantum number. The linear shift from the $B = 0$ states is known as the linear Zeeman shift. In the intermediate regime, the correction to the linear shift can be expressed in terms of and energy correction to each hyperfine state $\epsilon(B)|m_F|^2$,
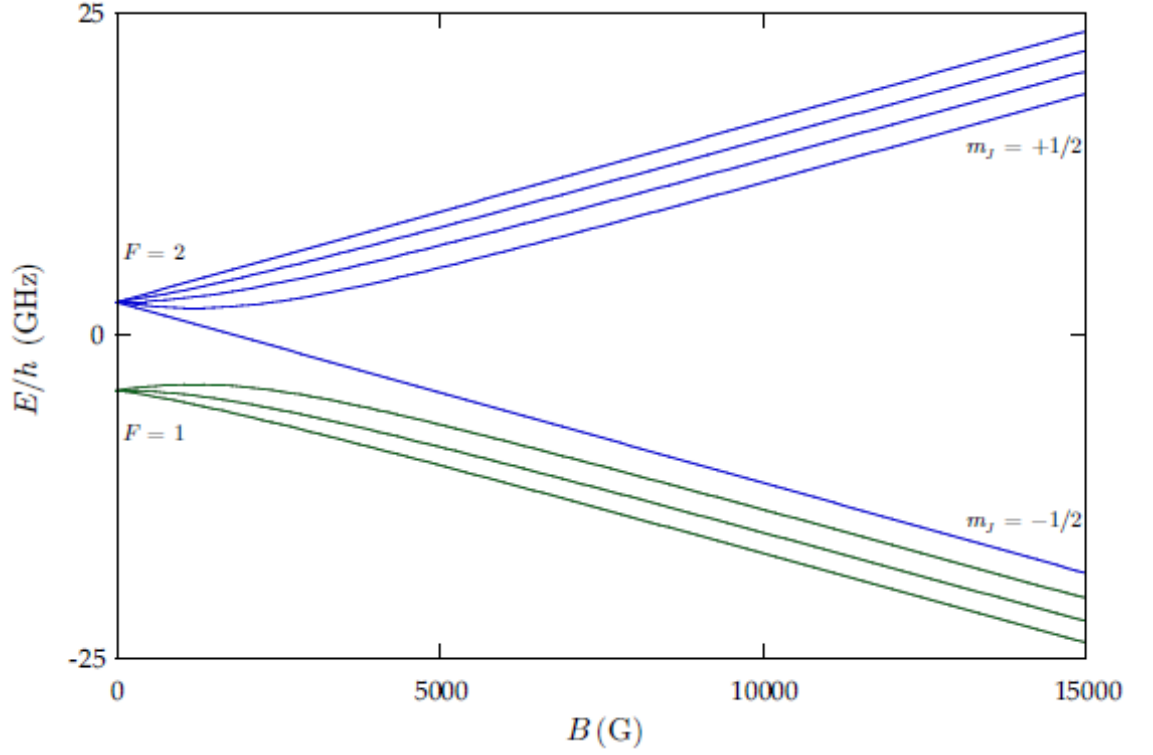
Figure 6: Energy structure of hyperfine states of the ground state of ^{87}Rb as a function of external magnetic field strength in Gauss. Figure from ref. [4]

known as the quadratic Zeeman shift. For the magnetic fields used in experiments described in this thesis, this correction is sufficient for describing the energy levels.

The form of the Hamiltonian in this regime for any value of F is given by

$$H_0 = H_{\text{KE}} + \hbar\omega_z \mathbf{F_z} + \hbar\epsilon \mathbf{F_z}^2, \tag{2.26}$$

where $\hbar\omega_z = \mu_B g_F B_z/\hbar$, and the kinetic energy Hamiltonian $H_{\text{KE}} = \hbar^2 \vec{k}^2/2m\mathcal{I}$, and $\mathcal{I}$ is the identity matrix.

2.4.2 Rf coupling Hamiltonian

For the $F = 1$ manifold, there are three available spin states $m_F = 0, \pm 1$. There are many ways of introducing coupling terms between the different hyperfine states. Here, we will explain two methods: rf coupling and Raman coupling. Rf coupling is a radio-frequency oscillating magnetic field, in our case produced by a pair of circular coils in series side by side above the atoms (see [5]). Assuming the rf oscillating field is polarized along the $\mathbf{e}_x$, with the bias field along $\mathbf{e}_z$, the coupling Hamiltonian is given by $H_{rf} = \mu_B g_F \vec{\mathbf{F}} \cdot \vec{B} = \mu_B g_F \mathbf{F}_x B_x \cos(\omega t)$, where $2\pi\omega$ is the rf frequency. The schematic of this setup is shown in Figure 7. The eignestates of the bare Hamiltonian H_0 are the constituent m_F states. The eigenstates of the coupled Hamiltonian $H_0 + H_{rf}(t)$ can be expressed as a linear superposition of the bare eignestates $\Psi(\vec{x}, t) = \sum_{m_F} c_{m_F}(t) \phi_{m_F}(\vec{x}) e^{-i\omega_{m_F} t}$. The Hamiltonian in this basis can then be written as [1]

$$
H_{\text{rf}} = H_{\text{KE}} + \hbar \begin{pmatrix} 0 & \Omega\cos(\omega t)e^{i\omega_z t} & 0 \\ \Omega\cos(\omega t)e^{-i\omega_z t} & 0 & \Omega\cos(\omega t)e^{i\omega_z t} \\ 0 & \Omega\cos(\omega t)e^{-i\omega_z t} & 0 \end{pmatrix}, \qquad (2.27)
$$

where Ω is the Rabi frequency, proportional to B_x. We can then transfer into the rotating frame $c'_{m_F} = e^{-im_F \delta t} c_{m_F}$, where $\delta = \omega_z - \omega$. Then we apply the rotating wave approximation, that the fast oscillating terms average to zero over time scales of interest $e^{2i\omega t} \approx 0$, and obtain

$$
H_{\text{rf}} = H_{\text{KE}} + \hbar \begin{pmatrix} \delta & \Omega/2 & 0 \\ \Omega/2 & -\epsilon & \Omega/2 \\ 0 & \Omega/2 & -\delta \end{pmatrix}, \qquad (2.28)
$$

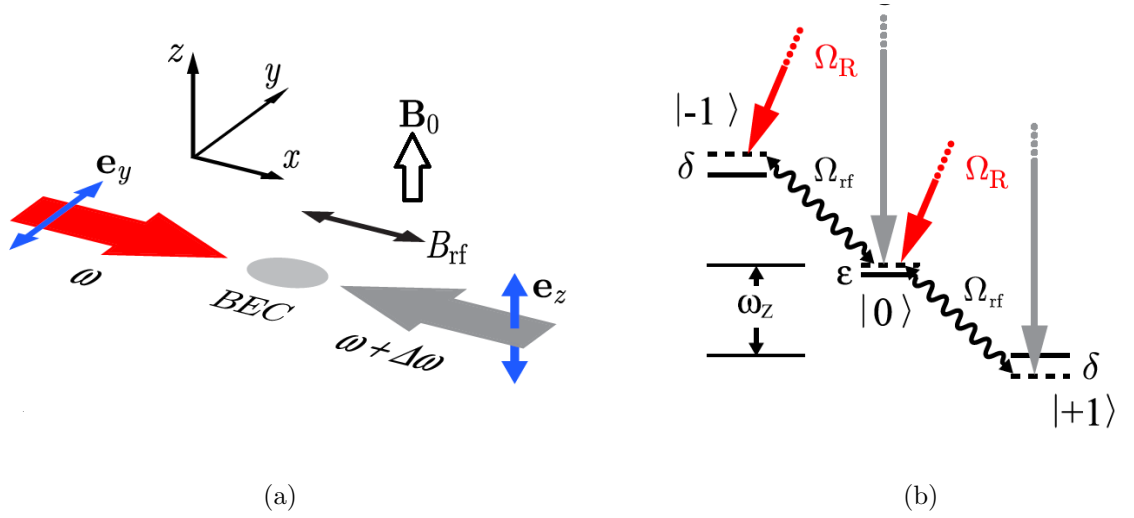(a)   (b)

Figure 7: Raman and rf coupling schematic. (a) Beam geometry of the Raman beams and rf relative to the external field. The Raman beams have a frequency difference $\Delta\omega$, and are linearly polarized in perpendicular directions. (b) Level structure of both Raman and Rf coupling for hyperfine states of the $F = 1$ manifold. The hyperfine splitting sparates the levels by an energy $\hbar\omega_z$. The quadratic Zeeman shift ϵ lowers the energy of the $m_F = 0$ state, and the detuning δ of either the Raman or the rf fields shifts the energies of the $m_F = \pm1$ states. Raman transitions are two-photon, exciting up to a virtual state and coming back down to an adjacent hyperfine state, with an accompanying momentum transfer. Rf couples adjacent hyperfine states directly. Figure taken from ref. [6]

or for any value of F

$$H_{\mathrm{rf}} = H_{\mathrm{KE}} + \hbar\delta F_z + \hbar\epsilon F_z^2 + \Omega F_x/2. \tag{2.29}$$

The band structure of this Hamiltonian can be seen in Figure 8, where we have diaganolized Eq. 2.28 for a range of momenta k_x (we have islolated k_x for comparison with Raman coupling, as will be seen in the next section). The parabolas are simply the free particle dispersion relations along one dimension, with three bands arising from the three available spin states. It is convenient to define the magnetization of an eigenstate $m = \sum_{m_F} m_F * p_{m_F}$, where p_{m_F} is the fractional population in the m_F state. We have indicated the magnetization of the eigentate by coloring the

eigenenrgies, with $m = -1$ in red, $m = 0$ in green, and $m = +1$ in blue. In Figure 8a, both the detuning and the coupling strength are zero. Therefore, there are simply three free particle dispersions, each exactly correlated with a particular spin state, the $m_F = \pm 1$ are degenerate and the $m_F = 0$ state is slightly offset by the quadratic shift $\hbar\epsilon$. In Figure 8c, the coupling strength is again zero, but the detuning has been turned on, lifting the degeneracy between the $m_F = \pm 1$ states. Figure 8b,d shows the same conditions as a,c, respectively, but with the coupling strength turned on. In Figure 8b, where the detuning is zero and the quadratic shift is negligible compared to the coupling strength, all states average to a magnetization of zero–the $m_F = \pm 1$ states are symmetrically populated. In Figure 8d, this symmetry is broken by the presence of a detuning.

2.4.3 Raman coupling Hamiltonian

The counter-propagating Raman beams, as seen in Figure 7, couple the same states as the rf. The do so via the vector light shift created by the pair of beams. The electric field due to the right going beam (red in Figure 7a) is $\mathbf{E} = E_0\exp(ik_Rx - i\omega t)\mathbf{e}_y$, where E_0 is the amplitude of the electric field and $\hbar k_R = h/\lambda_R = \hbar\omega/c$. The electric field from the left going beam (gray in Figure 7b) is $\mathbf{E} = E_0\exp(-ik_Rx - i(\omega + \Delta\omega)t)\mathbf{e}_z$. This combines to give an effective field from the vector light shift [7] $B_{\text{eff}} \propto \mathbf{E} \times \mathbf{E}^* \propto -E_0^2\cos(2k_Rx + \Delta\omega t)\mathbf{e}_x$. Going through the same procedure as for the rf coupling case, including the transfer into the rotating frame and the rotating wave approximation, we obtain the same Hamiltonian in the basis of bare spin states $|-1\rangle, |0\rangle, |1\rangle$ but with an extra phase factor:

$$H_{\text{Raman}} = H_{\text{KE}} + \hbar \begin{pmatrix} \delta & \Omega/2e^{-i2k_Rx} & 0 \\ \Omega/2e^{i2k_Rx} & -\epsilon & \Omega/2e^{-i2k_Rx} \\ 0 & \Omega/2e^{i2k_Rx} & -\delta \end{pmatrix}, \qquad (2.30)$$
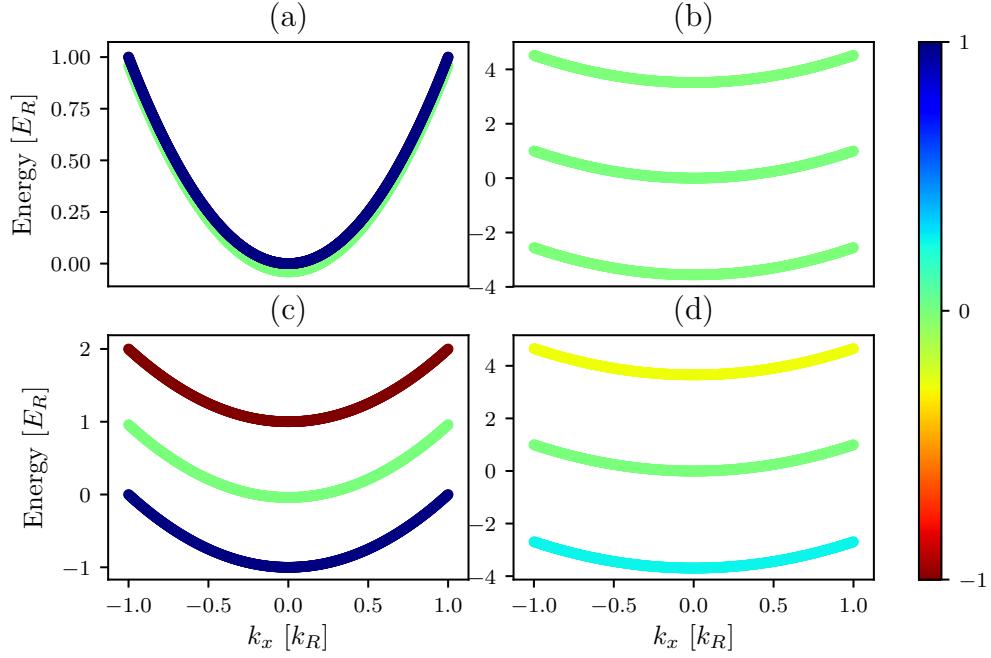
Figure 8: Band structure of the rf Hamiltonian, Eq. 2.28, in momentum space. For all plots, the quadratic Zeeman shift $\hbar\epsilon = 0.04E_R$, and the color represents magnetization, labeled by the colorbar. (a) $\hbar\Omega = 0$, $\hbar\delta = 0$. No coupling or detuning is present, so the only separation between the bands is due to the quadratic shift $\hbar\epsilon$. (b) $\hbar\Omega = 5.0E_R$, $\hbar\delta = 0$. (c) $\hbar\Omega = 0$, $\hbar\delta = 1.0E_R$. Even though the coupling strength is zero, the bands are separated by the detuning. (d) $\hbar\Omega = 5.0E_R$, $\hbar\delta = 1.0E_R$.

where $\delta = \omega_z - \Delta\omega$.

This phase difference between the rf and Raman Hamiltonian has an intuitive physical explanation. In order to undergo a Raman transition, an atom first absorbs a photon from one beam, getting a momentum kick equal to the recoil momentum $\hbar k_R$. Then, to decay back down to an adjacent spin state, the undergoes stimulated emission into the field of the other (counter-propagating) beam, acquiring another recoil momentum kick in the same direction for a total of $2\hbar k_R \mathbf{e}_x$. Therefore, the Raman coupling Hamiltonian for $F = 1$, after transforming into the rotating frame and performing the rotating wave approximation, can be written in the same way as the rf Hamiltonian in Eq. 2.28 with the addition of a momentum kick—in real space, an aquired phase—of $e^{i2k_R x}$.

We can again make a basis transformation to get rid of this phase. Let us define $|-1\rangle' = \exp(-2ik_R x)|-1\rangle = |k_x - 2k_R, -1\rangle$, $|0\rangle' = |0\rangle = |k_x, 0\rangle$, $|1\rangle' = \exp(2ik_R x)|1\rangle = |k_x + 2k_R, 1\rangle$, where for third definition we went into the momentum basis and labelled the states by a combination of their momentum and spin state. Then, including the kinetic energy term along $\mathbf{e}_x$ explicitly, we obtain the Hamiltonian in the new basis as:

$$H_{\text{Raman}} = H_{\text{KE}}^{(y,z)} + \begin{pmatrix} \frac{\hbar^2(k_x - 2k_R)^2}{2m} + \hbar\delta & \hbar\Omega/2 & 0 \\ \hbar\Omega/2 & \frac{\hbar^2 k_x^2}{2m} - \hbar\epsilon & \hbar\Omega/2 \\ 0 & \hbar\Omega/2 & \frac{\hbar^2(k_x + 2k_R)^2}{2m} - \hbar\delta \end{pmatrix}. \quad (2.31)$$

It is convenient to define the Raman recoil energy as $E_R = \frac{\hbar^2 k_R^2}{2m}$. The band structure of this Hamiltonian is shown in Figure 9, for several representative parameter values, with the magnetization labelled by the color. Figure 9a shows the band structure in the limit of zero coupling and zero detuning, but where we have already gone into the basis $|k_x - 2k_R, -1\rangle$, $|k_x, 0\rangle$, $|k_x + 2k_R, 1\rangle$; therefore, the free particle parabola corresponding to the $m_F = 1$ spin states is shifted to center on

$k_x = -2k_R$ and the $m_F = -1$ parabola is shifted to center on $k_x = 2k_R$. As the coupling is turned on to $\hbar\Omega = 1E_R$ in Figure 9b, the points where the parabolas cross become 'avoided crossings', separating into three bands where magnetization (and the underlying spin distribution) depends on the momentum k_x. As the coupling strength is turned up even further to $\hbar\Omega = 5E_R$ in Figure 9c, the lowest band goes from having three minima, one corresponding to each original spin state, to only one minimum. This transition happens at $\hbar\Omega = 4E_R$ [5]. In Figure 9d, we show the band structure again in the limit of zero coupling, but this time with a detuning of $\hbar\delta = 1.0E_R$. Note that the detuning tips the parabolas with respect to each other. Figure 9e shows the detuned system with coupling strenth turned up to $\hbar\Omega = 1E_R$, still in the three minima regime but with avoided crossings creating three momentum and spin coupled bands. In Figure 9f, the detuned system is turned up to a coupling strength of $\hbar\Omega = 5E_R$, creating a single minimum, this time offset from $k_x = 0$.

We can write the general F version of the Raman coupled Hamiltonian in the basis $|k_x + m_F * 2k_R, m_F\rangle$, where $-F \leq m_F \leq F$, as:

$$H_{\text{Raman}} = H_{\text{KE}}^{(y,z)} + \hbar^2(k_x\mathcal{I} + 2k_R F_z)^2/2m + \hbar\delta F_z + \hbar\epsilon F_z^2 + \Omega F_x/2. \qquad (2.32)$$

2.4.4 Calibration of Raman and Rf dressed states

To calibrate the rf and Raman coupling strengths, we take a similar approach to the 1-D lattice calibration: start in a pure spin state, for example $m_F = 0$, and turn the coupling on non-adiabatically to induce Rabi oscillations between the coupled states. Then, during time-of-flight, apply a Stern-Gerlach gradient pulse to separate the spin compoenets and observe the fractional populations in different spin states as a function of Rabi oscillation time.

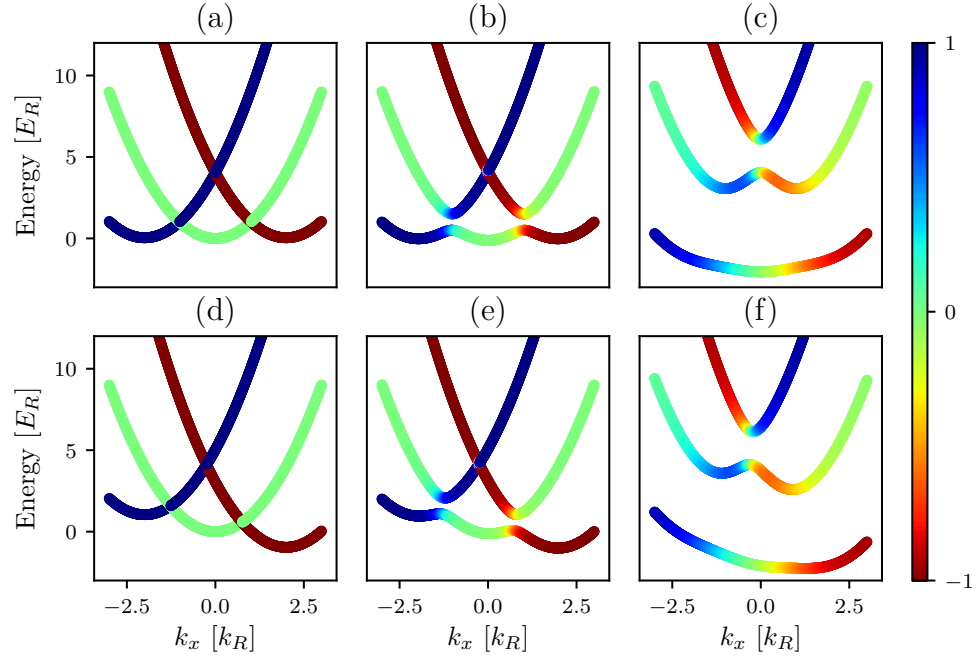Figure 10a,b shows example images obtained in time-of-flight when pulsing on

Figure 9: Band structure of the Raman Hamiltonian, Eq. **??**, in momentum space. For all plots, the quadratic Zeeman shift $\hbar\epsilon = 0.04E_R$, and the color represents magnetization, labeled by the colorbar. (a) $\hbar\Omega = 0$, $\hbar\delta = 0$. (b) $\hbar\Omega = 1.0E_R$, $\hbar\delta = 0$. (c) $\hbar\Omega = 5.0E_R$, $\hbar\delta = 0.0$. (d) $\hbar\Omega = 0.0$, $\hbar\delta = 1.0E_R$. (e) $\hbar\Omega = 1.0E_R$, $\hbar\delta = 1.0E_R$. (f) $\hbar\Omega = 5.0E_R$, $\hbar\delta = 1.0E_R$

an rf coupling field for atoms in the $F = 1$ and $F = 2$ manifold, respectively. The Stern-Gerlach gradient pulse separates the spin components along the horizontal axis in the images. The fractional population in each state can then be obtained by summing up the optical depth in each cloud and dividing by the total optical depth. Similarly, Figure 11a shows an example time-of-flight image obtained when pulsing on a Raman coupling field on an $F = 1$ cloud initially in the $m_F = 0$ spin state. Here, the spin states are separated along the horizontal axis by the same Sternch-Gerlach pulse. In addition, the recoil momentum obtained when undergoing a Raman transition separates the different spin states along the vertical axis— parallel to the Raman beams along $\mathbf{e}_x$. The direction of the Stern-Gerlach gradient was chosen purposefully to be perpendicular to the Raman direction $\mathbf{e}_x$ for easy separation of the two effects.

These population oscillations can then be fit for coupling strength $\hbar\Omega$ and detuning $\hbar\delta$ Note that the quadratic Zeeman shift $\hbar\epsilon$ is set by the strength of the bias field B_0 and therefore often well known - we do not fit for this. The theoretic predictions are obtained by applying the time evolution operator $U = \exp(-iH_{\mathrm{Raman/rf}}t/\hbar)$ to an initial state Ψ in the appropriate basis. Figure 10c shows an example time series of rf pulsing in the $F = 1$ maifold, starting in the $m_F = 0$ state. The lines of best fit are overlaid on experimental data, extracting fit parameters $\hbar\Omega = 0.863 \pm 0.004 E_R$ and $\hbar\delta = -0.198 \pm 0.007 E_R$. Figure 10d shows an example time series of rf pulsing in the $F = 2$ maifold, starting in the $m_F = -2$ state. Here, the extracted fit parameters were $\hbar\Omega = 1.000 \pm 0.002 E_R$ and $\hbar\delta = -0.061 \pm 0.001 E_R$.

Figure 11b shows an example time series of Raman pulsing in the $F = 1$ manifold, starting in the $m_F = 0$ state, with fitted parameters $\hbar\Omega = 1.47 \pm 0.01 E_R$ and $\hbar\delta = 0.004 \pm 0.024 E_R$. Note that although the coupling strength is almost double the rf coupling strenth in Figure 10c, the contrast (peak to peak oscillation
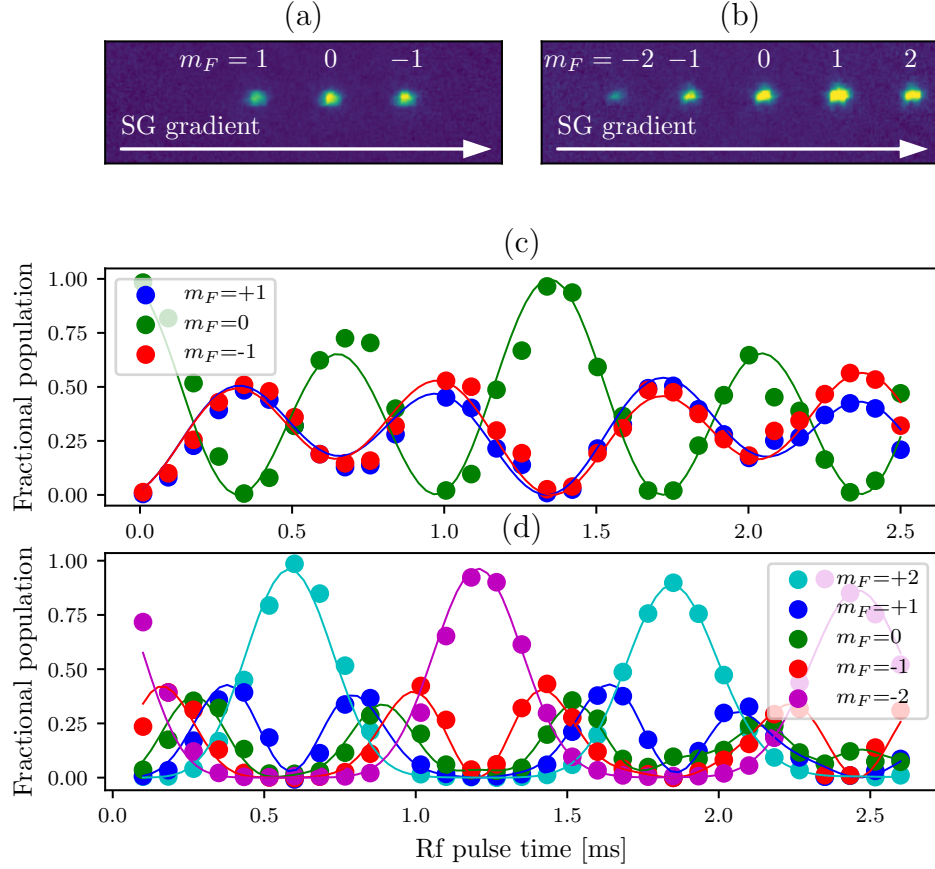
Figure 10: Pulsing on rf coupling. (a) Example time-of-flight image during an rf pusling experiment in the $F = 1$ manifold. Spin states are separated via a Stern-Gerlach pulse along the horizontal direction. (b) Example time-of-flight image during an rf pusling experiment in the $F = 2$ manifold. Here, 5 spin components are present. (c) Pulsing experiment in the $F = 1$ manifold. Dots represent fractional populations in different spin states measured from time-of-flight images, and lines repressent best fit theory curves. Fitted parameters are $\hbar\Omega = 0.863 \pm 0.004E_R$, $\hbar\delta = -0.198 \pm 0.007E_R$. (d)Pulsing experiment in the $F = 2$ manifold. Dots represent fractional populations in different spin states measured from time-of-flight images, and lines repressent best fit theory curves. Fitted parameters are $\hbar\Omega = 1.000 \pm 0.002E_R$, $\hbar\delta = -0.061 \pm 0.001E_R$. $\hbar\epsilon = 0.038E_R$ for all panels.
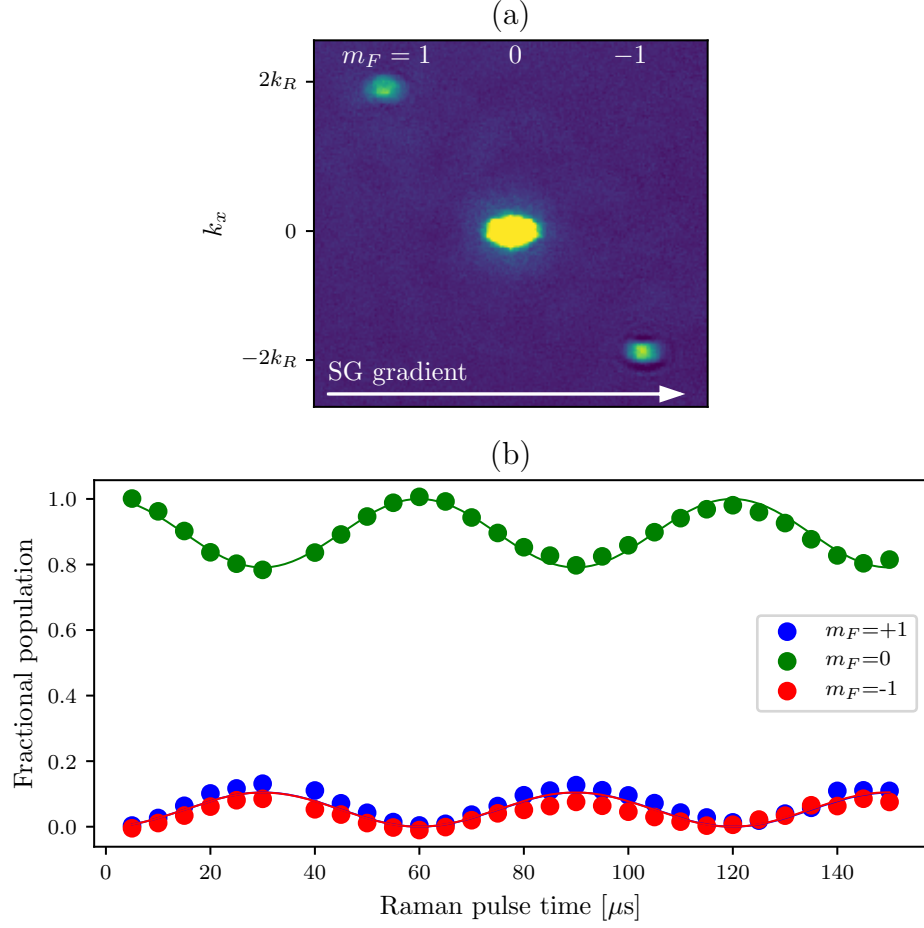
Figure 11: Pulsing on Raman coupling. (a) Example time-of-flight image during a Raman pulsing experiment in the $F = 1$ manifold. A Stern-Gerlach pulse during time-of-flight separates different spin components along the horizontal direction, and different momentum orders fly apart along the vertical direction. (b) Fractional population in different spin states during a Raman pulsing experiment as a function of time. Dots represent data and lines represent a best fit from theory. The fitted parameters are $\hbar\Omega = 1.47 \pm 0.01 E_R$, $\hbar\delta = 0.004 \pm 0.024 E_R$. The quadratic Zeeman shift was $\hbar\epsilon = 0.038 E_R$.

of the fractional population in, say, the $mF = 0$ state) is much lower in the Raman data than in the rf. This is a direct consequence of the recoil momentum transfer, and can be understood by looking at the band structure. For rf, the coupled bands at initial momentum $k_x = 0$ are separated by the coupling strength, see Figure ??b. For Raman, even at zero coupling strength, due to the shifting of the parabolas by $2k_R$, and $k_x = 0$ the higher bands are $\hbar^2 (2k_R)^2 / 2m = 4E_R$ separated from the lower bands. Therefore, the energy difference is larger and the fraction in the excited band will be lower, leading to lower contrast.

Chapter 3: Absorption Imaging with Recoil Induced Detuning

3.1 Recoil-induced detuning

After absorbing a number of photons N, an atom will obtain a recoil velocity of Nv_{r}. Via the Doppler effect, this will result in a detuning $\delta = Nk_{\mathrm{r}}v_{\mathrm{r}}$. This detuning will increase as more atoms are absorbed, and therefore depend on time, making the absorbed intensity also time dependent. We can generalize Eq. 2.3 to include a time dependence on the detuning term and therefore also the intensity:

$$\frac{d}{dz}\frac{I(z,t)}{I_{\mathrm{sat}}} = -\rho(z)\sigma_0\frac{I(z,t)/I_{\mathrm{sat}}}{1 + 4\delta(z,t)^2/\Gamma^2 + I(z,t)/I_{\mathrm{sat}}}. \tag{3.1}$$

The number of photons absorbed per atom will depend on the intensity lost, up until the current time, at that location. The detuning will therefore be proportional to the total number of photons lost up until time t at that location, proportional to the absorbed intensity divided by the single photon energy $\hbar\omega_L$, divided by the number of atoms that participated in the aborption $\rho(z)$ times the detuning $k_{\mathrm{r}}v_{\mathrm{r}}$:

$$\delta(t,z) = \frac{k_{\mathrm{r}}v_{\mathrm{r}}}{\hbar\omega_L\rho(z)}\int_0^t \frac{dI(z,\tau)}{dz}\mathrm{d}\tau. \tag{3.2}$$

These equations are interdependent, and cannot be in general solved analytically.

Figure 1a shows the velocity and detuning as a function of position in space for three different imaging times, calculated numberically. All calculations in this chapter were done for a cloud of ^{40}K atoms, as that is relevant to our experiment

described in the next chapter. The resonant wavelength is $\lambda_L = 770.11$ nm, the natural linewidth of the transition is $\Gamma = 6.035$ MHz, the resulting saturation intensity and recoil velocity are $I_{\text{sat}} = 17.5$ W/m^2 and $v_{\text{r}} = 0.01297$ m/s.

3.2 Perturbative treatment

We can treat these equations perturbatively in time. To first order, we can set the detuning in Eq. 3.1 to $\delta = 0$, assume $I(z)$ is time independent, and plug that into Eq. 3.2 to obtain

$$\delta(t,z) = \frac{k_{\text{r}} v_{\text{r}}}{\hbar \omega_L \rho(z)} \int_0^t -\rho(z) \sigma_0 \frac{I(z)}{1 + I(z)/I_{\text{sat}}} d\tau \tag{3.3}$$

$$= \frac{k_{\text{r}} v_{\text{r}} \sigma_0}{\hbar \omega_L} \frac{I(z)}{1 + I/I_{\text{sat}}} t. \tag{3.4}$$

This can then be recursively plugged into Eq. 3.1 to obtain

$$\frac{d}{dz} \frac{I(z,t)}{I_{\text{sat}}} = -\rho(z) \sigma_0 \frac{I(z,t)/I_{\text{sat}}}{1 + 4\left(\frac{k_{\text{r}} v_{\text{r}} \sigma_0}{\hbar \omega_L \Gamma} \frac{I(z)}{1 + I/I_{\text{sat}}}\right)^2 t^2 + I(z,t)/I_{\text{sat}}}. \tag{3.5}$$

Integrating both sides of the above equation, we obtain a perturbative equation to second order in time [8]:

$$\sigma_0 n = ln(I_0/I_f) + \frac{I_0 - I_f}{I_{\text{sat}}} + \frac{(k_{\text{r}} v_{\text{r}} t)^2}{3}\left(\frac{I_{\text{sat}}}{I_f + I_{\text{sat}}} - \frac{I_{\text{sat}}}{I_0 + I_{\text{sat}}} + \ln\left(\frac{I_f + I_{\text{sat}}}{I_0 + I_{\text{sat}}}\right)\right). \tag{3.6}$$

In Fig. 1b, we examine for what imaging times the above perturbative equation, as well as the modelt that completely ignores recoil induced detuning, is valid. We do this by performing numerical simulations to extract a value for the final intensity I_f and using Eq. 2.4 and Eq. 3.6 to extract values $\sigma_0 n$ that would be deduced from experimnet. We find that within the recoil time, both analytic expressions start to differ from the true atomic column density by over 5%, and the perturbative model
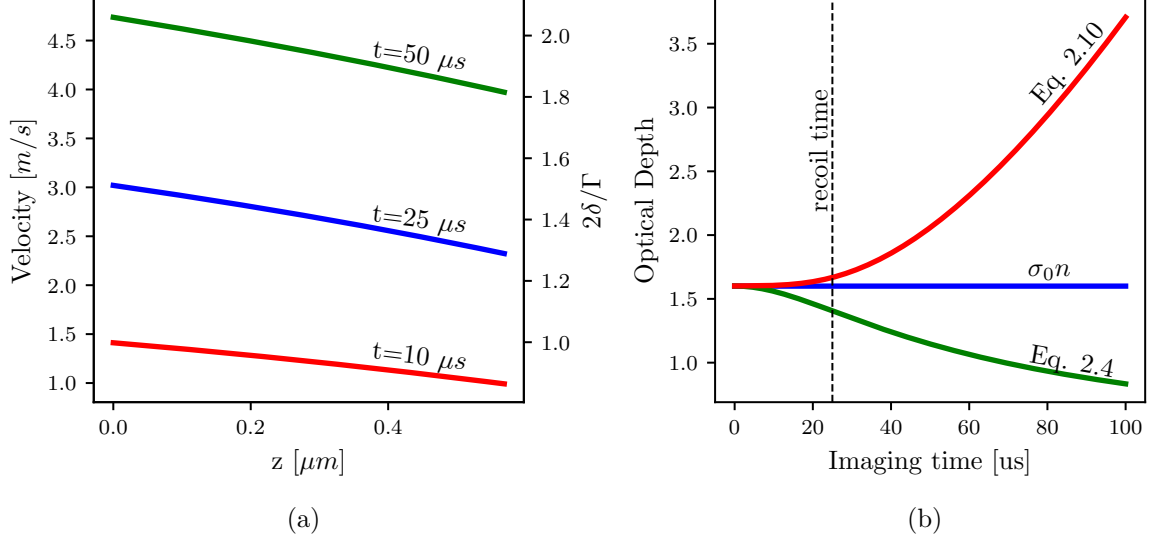
Figure 1: (a) Dependence of velocity and detuning on position simulated for ^{40}K at three different imaging times and a probe intensity $I_0 = 0.8I_{\text{sat}}$. (b) Column densities deduced from optical depths obtained from recoil detuning corrected simulation of on-resonant imaging of ^{40}K atoms at probe intensity $I_0 = 0.8I_{\text{sat}}$. The blue line is the input column density $\sigma_0 n = 1.6$. The green line is the high probe intensity corrected column density given by Eq. (2.4). The red line is the column density as expanded to second order in time, Eq. (3.6).

of Eq. 3.6 quickly divereges thereafter.

In the following sections, we describe two versions of numerical simulations that we have performed in order to appropriately extract atomic column densities from experimental data.

3.3   Stationary atom model

In order to numerically simulate the imaging process, we assume a Gaussian distribution of atoms along the propagation direction, $\rho(z) = n/sqrt2\pi w e^{(} - z^2/2w^2)$. The dependence of the result on the choice of cloud width w is discussed in the next chapter. We divide the cloud into small bins along z. For the initial version of the simulation, the atoms were assumed to stay within the same bins for

the entire duration of the imaging pulse, i.e. the cloud shape remained constant. We then used Eqs. 3.1-3.2 to numerically propagate the probe intensity and detuning as a function of both time and space. The algorithm used is detailed by Alg. 1.

Algorithm 1 Stationary atom model

$I[n = 0, t] = I_0$ {n is the bin index, t is the time index, I is in units of I_{sat}}
$\delta[n, t = 0] = 0$ {light initially resonant, δ in units of $\Gamma/2$}
$H_f = 0$ {Radiant fluence seen by camera after passing through cloud}
for $t = 0$ to t_f **do** {loop over time steps}
    for $n = 1$ to N **do** {loop over bins, N is total bin number}
        $A = \sigma_0 \rho[n] dz$ {dz is the size of spatial step}
        $B = v_r dt/(\hbar c \rho[n])$ {dt is the size of the time step}
        $I[n, t] = I[n - 1, t] - AI[n - 1, t]/(1 + \delta[n, t - 1]^2 + I[n - 1, t])$ {Eq. (3.1)}
        $\delta[n, t] = \delta[n, t - 1] + B\left(I[n - 1, t] - I[n, t]\right)$ {Eq. (3.2)}
    end for
    $H_f = H_f + I[N, t]dt$ {collecting total fluence seen by the camera}
end for
$OD^{\text{sim1}} = -\ln\left(H_f/I_0 t_f\right)$

We call the optical depth obtained in this way OD^{sim1}, to distinguish if from the simulated optical depth via the method described in the next section.

The validity of this model can be checked by considering limits where the equations are analytically solvable. For short imaging times, the recoil-induced detuning should not contribute to the optical depth, and therefore Eq. 2.4 should become exact. This is seen in Fig. 2a, where the imaging pulse is only 3 μs long and the simulated optical depth (blue dots) agrees with that given by Eq. 2.4 for all intensity regimes.

Even at longer imaging times, the problem can be analytically solved for limits of both high and low intensity compared to the saturation intensity. At intensities $I \gg I_{\text{sat}}$, even far detuned atoms will scatter light at their maximum, and we can assume $\delta^2/\Gamma^2 \ll I/I_{\text{sat}}$, reducing back to Eq. 2.4. At extremely low intensities, atoms will scatter very little light and the detuning $\delta^2/\Gamma^2 \ll 1$, again reducing back to Eq. 2.4. As seen in Fig. 2 b,c the simulation agrees with the analytic Eq. 2.4 in the limit of both high and low intensities. But, as the imaging time increases, the
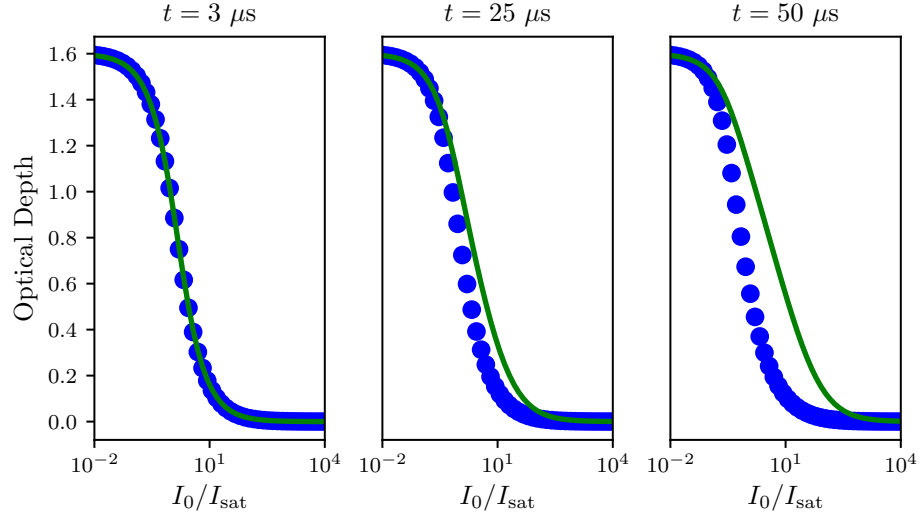
Figure 2: Optical depth as a function of probe intensity as predicted by the simulation (blue symbols) and by Eq. (2.4) (green curves), for three different imaging times. As expected, the predictions agree in both the high and low intensity limits, and differ for probe intensities comparable to the saturation intensity and longer imaging times.

disagreement due to recoil induced detuning grows.

The simulation allows us to extract both the intensity and the detuning as a function of both time and position. We can use this information to infer the velocity and therefore the displacement of the atoms during the imaging pulse, and check if our assumption that the atoms stay in their original 'bins' during the image pulse is valid. Figure 3a shows the position, deduced by integrating the recoil-induced velocity, as a function of time of the first, middle, and last spatial 'bin' for a probe intensity slightly above saturation, $I = 1.2I_{\text{sat}}$. As seen in the figure, not only do the atoms move beyond their 'bins', but also at long imaging times the first atoms (which have absorbed the most light) overtake the last ones. Therefore, the atomic cloud does not maintain shape during the imaging pulse, and our initial assumption is invalid.
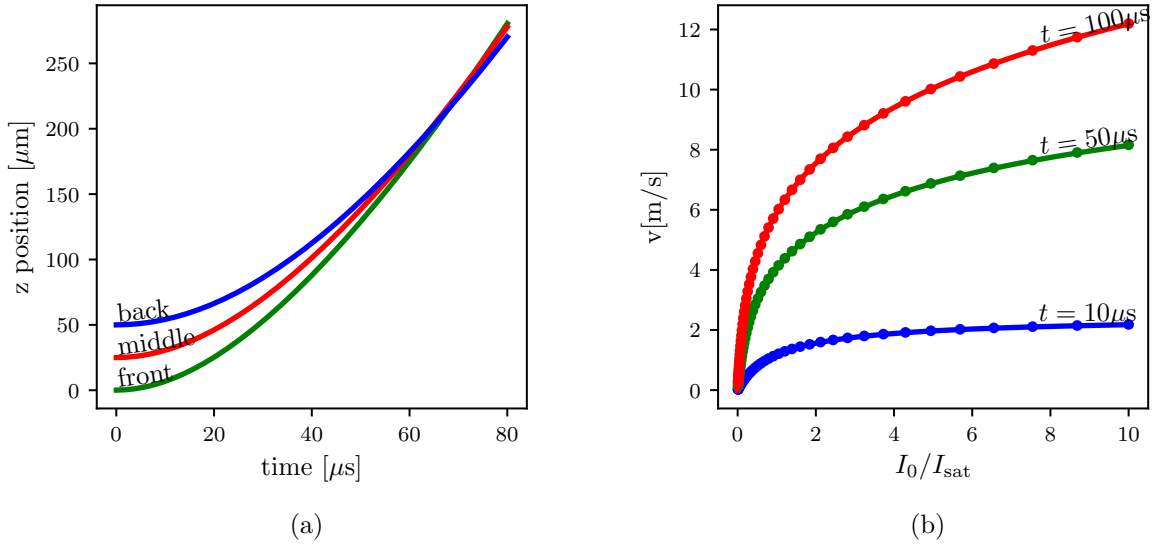
Figure 3: (a) Position of atoms as a function of imaging time for atoms in the first (solid green), middle (dashed red), and last (dotted blue) bins of the simulated density distribution for an initial cloud 50 μm in extent. The probe intensity used in this calculation was $1.2\,I_{\text{sat}}$, and the column density was $\sigma_0 n = 1.6$. (b) The velocity of a single composite atom as a function of probe intensity for various imaging times. Simulation data (dots) and numerical solutions of Eq. (3.7) (lines) are in agreement.

3.4 Traveling atom model

To model the recoil-induced detuning effect during the imaging pulse taking into account the potentially significant spatial displacement of the atoms, we performed a second version of our simulation. In this version, we clumped some number of atoms N_{ca} into a single composite atom, and then tracked the detuning, velocity and position of each composite atom as a function of imaging time. Tacking individual atoms would be computationally inaccessible for reasonable cloud sizes. The algorithm used is given by Alg. 2.

Algorithm 2 Travelling atom model

$z[n] = z_0$, $\delta[n] = 0$ {initialize position and detuning for each composite atom, labeled by index n}
$O[i] = n$ {make a list of composite atom indexes, ordered by position}
$I[n = 0, t] = I_0$ { t is the time index, I is in units of I_{sat}}
$H_f = 0$ {Radiant fluence seen by camera after passing through cloud}
for $t = 0$ to t_f **do** {loop over time steps}
  for $i = 1$ to N **do** {loop over superatoms}
    $n = O[i]$ {apply probe intensity to composite atoms in order of appearance}
    $A = \sigma_0 N_{sa} dz$ {dz is length over which atoms were grouped into single composite atom}
    $B = v_r dt / (\hbar c N_{sa})$ {dt is the time step}
    $I[n, t] = I[n-1, t] - AI[n-1, t] / (1 + \delta[n]^2 + I[n-1, t])$ {Eq. (3.1)}
    $\delta[n] \mathrel{+}= B \left(I[n-1, t] - I[n, t] \right)$ {Eq. (3.2), detuning in units of $\Gamma/2$}
    $z[n] \mathrel{+}= dt \Gamma \delta / 2k$ {k is the wavenumber, $\Gamma\delta/2k$ is the velocity at δ detuning}
  end for
  $O[i] = \mathrm{sort}(n, \mathrm{key} = z[n])$ {sort composite atom indexes by current position}
  $H_f H_f + I[N, t] dt$ {collecting total fluence seen by the camera}
end for
$OD^{\mathrm{sim2}} = -\ln\left(H_f / I_0 t_f \right)$

To check the validity of this version of the simulation, we check the velocity of a composite atom as a function of time in an analytically solvable limit. In this case, we take the limit of a single composite atom, such that the intensity seen by the composite atom becomes time independent. This simplifies Eqs. 3.1 and 3.2 to only carry time dependence in the detuning term, and we can then plug Eq. 3.1

into Eq. 3.2 and differentiate both sides with respect to time to obtain

$$\frac{d\delta(t)}{dt} = \frac{\Gamma k_r v_r}{2} \frac{I/I_{\text{sat}}}{1 + 4\delta^2/\Gamma^2 + I/I_{\text{sat}}}. \tag{3.7}$$

Equation (3.7) can be solved numerically, and is in agreement with our simulation, as seen in Fig. 3(b).

We then used this version of the simulation to look at the motion of composite atoms as a function of imaging time in phase space (ie, velocity and position). Some examples of this motion can be seen in Fig. 4. As seen in the figure, the atomic cloud is significantly distorted during the imaging pulse and the atoms perform some crazy acrobatics.

It remains to check how the atoms' acrobatics affect the resulting optical depth, ie the attenuation of the probe beam. To do this, we compare the optical depths generated by our stationary atom model, OD^{sim1}, and by our travelling atom model, OD^{sim2}. The results of this comparison are seen in Fig. 5(a). As seen from the figure, the optical depths predicted by the two versions of the simulation are negligibly small - $\left| OD^{\text{sim1}} - OD^{\text{sim2}} \right| / OD^{\text{sim1}} \leq 0.005$. We also checked the effect of having different initial distributions of atoms in space by varying the initial function $\rho(z)$ and keeping the total atom number constat. We found the effect of this to be negligible as well. Therefore, to infer atomic column densities from observed optical depths, it is sufficient to use the satationary atom model.

3.5   Calibration of saturation intensity

Saturation intensity is an intrinsic propety of the atom, so the idea of calibrating it may be confusing. However, there are several experimental parameters that may influence exactly what value of I_{sat} is appropriate to use in Eq. 3.1 and 3.2, such as losses in the imaging system and polarization of the probe beam. In
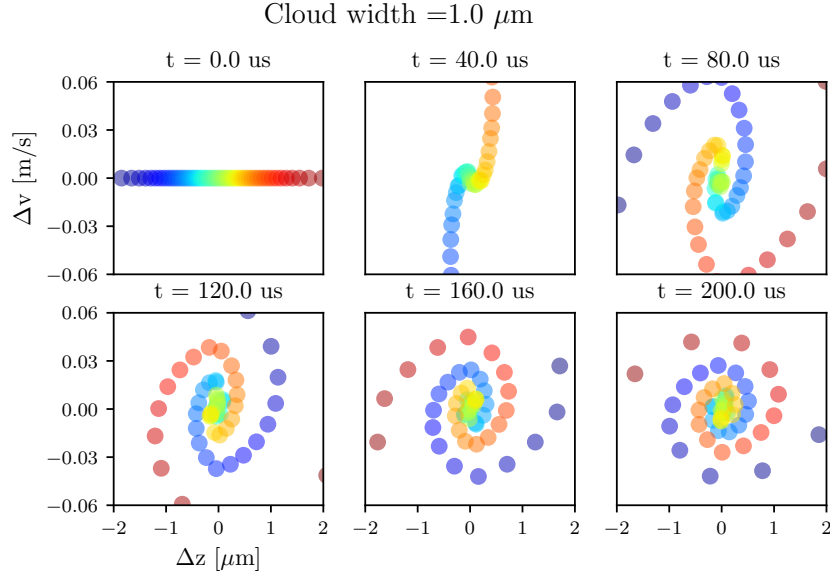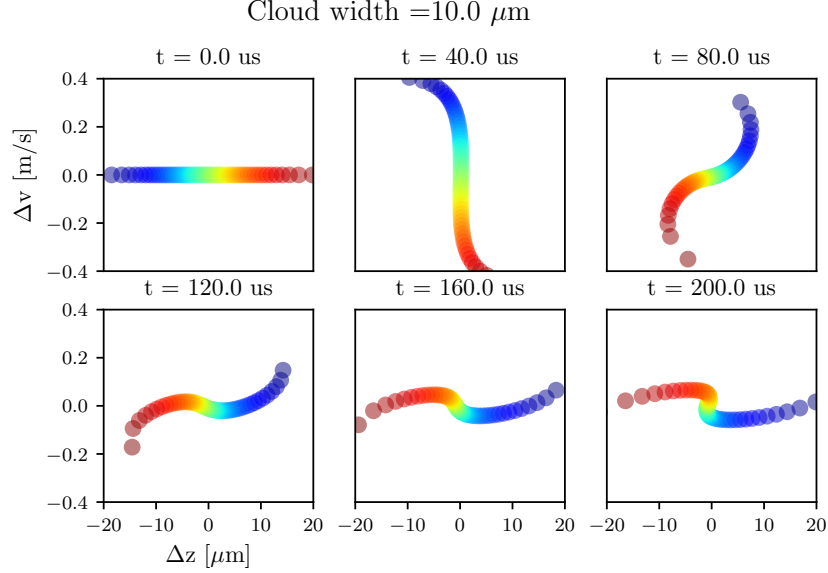
Figure 4: Phase space evolution of an atomic cloud exposed to probe light with intensity $\tilde{I}_0 = 1.2$. We defined $\Delta v = v - \langle v(t) \rangle$ and $\Delta z = z - \langle z(t) \rangle$, subtracting out the center of mass position and velocity of the cloud. The column density $\sigma_0 n$ is 1.6, and the initial cloud is a Gaussian with a width of 10 μm in (a) and 1 μm in (b). The center of mass velocities $\langle v \rangle$ are (0, 3.41, 5.26, 6.52, 7.50, 8.32) m/s sequentially, and are the same for both initial cloud widths.
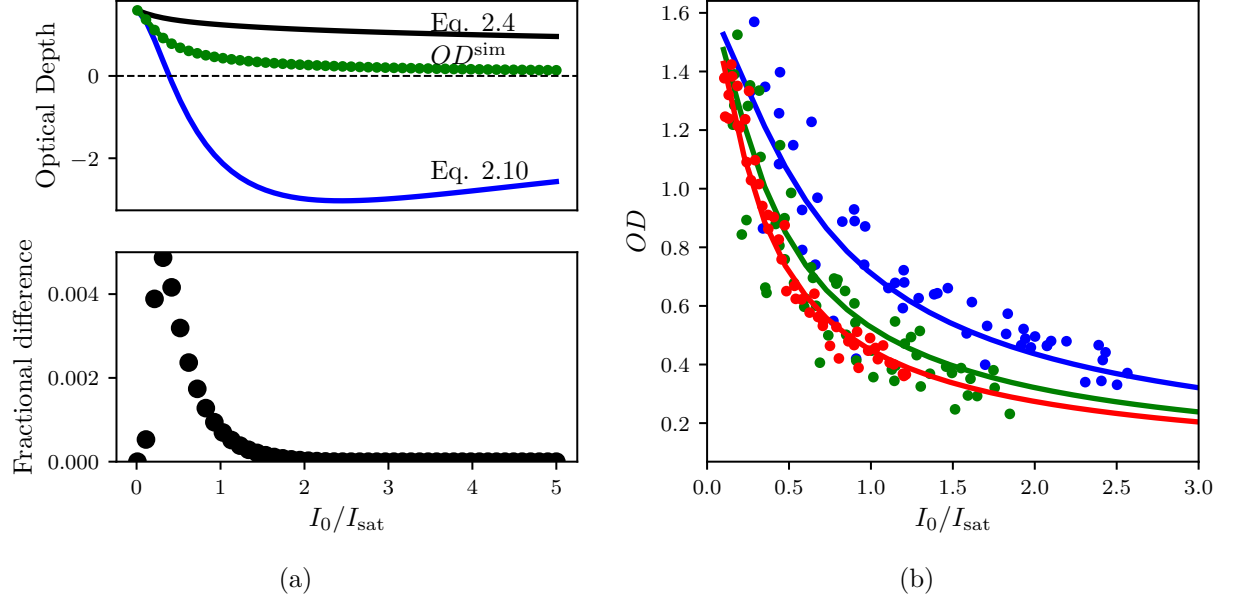
Figure 5: (a) Top. Optical depth as a function of probe intensity for an imaging time $t = 100$ μs. $OD^{(1)}$ and $OD^{(2)}$ are optical depths predicted from a given column density by Eq. (2.4) and (3.6) respectively. The two versions of simulated optical depth, OD^{sim1} (green curve) and OD^{sim2} (green dots) are plotted. Bottom. The fractional difference between two versions of the simulated OD, $\left|OD^{\mathrm{sim1}} - OD^{\mathrm{sim2}}\right|/OD^{\mathrm{sim1}}$. (b) The optical depth as a function of probe intensity for three imaging times: $t = 40$ μs (cyan), $t = 75$ μs (magenta), $t = 100$ μs (red). The dots represent experimental data and the lines represent the best fit of simulated data. The optimal fit parameters pictured are a $\sigma_0 n$ of 1.627(5) and saturation intensity of 29(7) counts/μs.

addition, we have no direct experimental access to the total radiant fluence (time integral of intensity) seen by the camera. Instead, the light hitting the charge-coupled device (CCD) camera triggers some number of photoelectrons to be registered. The proportionality between the number of photons hitting the camera and the number of photoelectrons it triggers is called the quantum efficiency q_e of the camera. The number of these photelectrons, after some electronic gain and noise introduced during the readout process, is then read out as a number of 'counts' registered on each pixel. The camera-dependent factors influencing how the number of counts depends on the number of incoming photons can be convolved with the experimental factors of probe polarization and optical loss into a single calibration of the effective saturation intensity in units of 'counts' output by the camera per unit time.

To calibrate this effective I_{sat} in camera counts per unit time, we absorption imaged our cloud of ^{40}K atoms for a range of probe intensities for three different values of imaging time: 40 μs, 100 μs, and 200 μs. We select a small region in the center of the cloud, where we can assume the atomic column density $\sigma_0 n$, and the initial probe intensity I_0 to be roughly constant. We then average the values of I_0 and I_f over this region and plot the final intensity I_f as a function of I_0. We then used the optical depth predicted by our simulation OD^{sim} and used that to simultaniously fit the three curves with I_{sat} and $\sigma_0 n$ as fit parameters, as shown in Fig. 5(b). As can be seen from the figure, this procedure not only allows us to read off I_{sat} in units of camera counts per μs, but also shows that our simulation accurately reproduces the differences in OD dependenc on imaging time.

3.6   SNR optimization

Using the simulations described in the previous sections, we can create a lookup table of atomic column densities as a function of initial and final probe intensities I_0 and I_f for any given imaging time. This lookup table can be then used to interpret

experimental data and obtain the atom number in regimes where the recoil-induced detuning is significant. This procedure can also be used to propagate photon shot noise into uncertainty in measured atom number.

We consider Poisson distributed photon shot noise, converting into shot noise on photoelectrons triggered inside the CCD. The standard deviation will then be proportional to $q_{\mathrm{e}}\sqrt{N_p}$, where q_{e} is the quantum efficiency of the camera and N_p is the photon number. This uncertainty can be then propagated via the lookup table into uncertainty on the measured atomic column density $\delta_{\sigma_0 n}$. The signal to noise ratio (SNR) can then be expressed as $\sigma_0 n / \delta_{\sigma_0 n}$.

We study the SNR as a function of imaging time and initial probe intensity for a few different atomic column densities. Some representative data is shown in Fig. 6. As seen in Fig. 6(a), for a wide range of atomic column densities, extending the imaging time beyond 40 μs no longer yields significant improvements in SNR. There is, however, a factor of 1.5 improvement between using an imaging time of 10 μs, where the simple model given by Eq. 2.4 is appropriate, and 40 μs. Therefore, there are signifiant gains that can be made by going to longer imaging times and making use of the simulated lookup table.

This simulation allowed us to interpret experimental data. For a given imaging time, we created a look-up table of predicted optical depth as a function of probe intensity and atomic column density. We then found the observed optical depth on this table, with the given probe intensity, and inferred the atomic density. The uncertainty in the measured intensities can be propagated through this procedure, and we established optimal imaging parameters to maximize the SNR of this detection scheme. Figure 6(b) illustrates that the optimal initial probe intensity is different for different atom numbers. For low atom numbers, $\sigma_0 n \approx 0.1$, a probe intensity of $I_0 \approx 0.6 I_{\mathrm{sat}}$ is best.
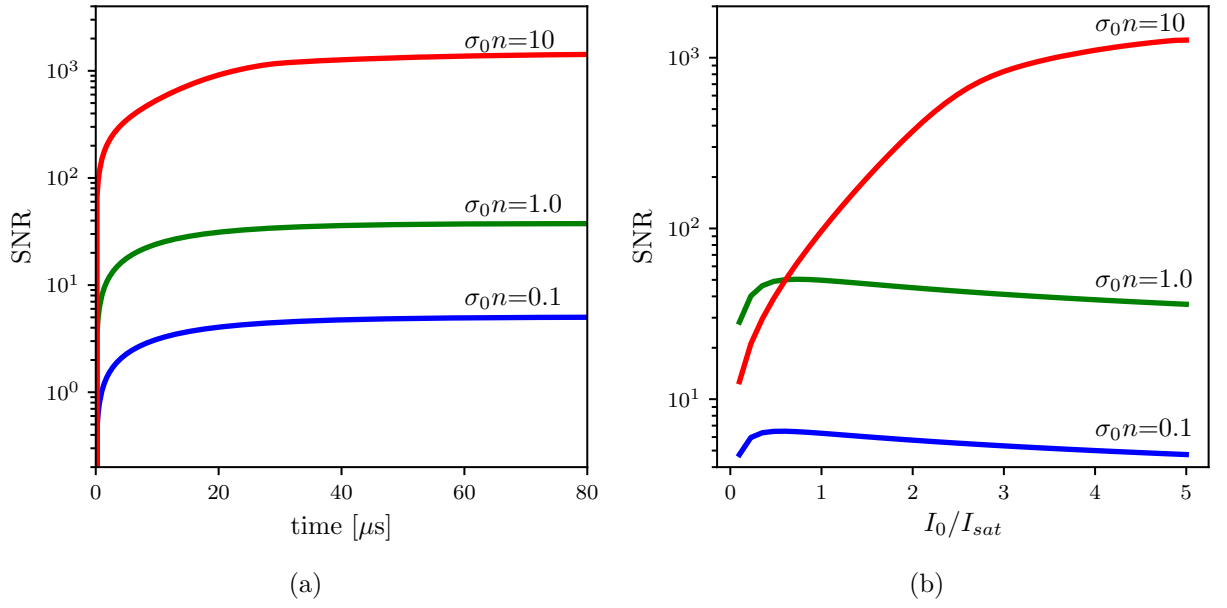
Figure 6: SNR for three different column densities after correcting for recoil induced detuning. (a) SNR as a function of imaging time for a probe intensity of $I_0 = 5.0 I_{\text{sat}}$ and (b) SNR as a function of probe intensity for an imaging time of 50 μs.

Bibliography

[1] H.J. Metcalf and P. van der Straten. *Laser Cooling and Trapping*. Graduate Texts in Contemporary Physics. Springer New York, 1999.

[2] N.W. Ashcroft and N.D. Mermin. *Solid State Physics*. Saunders College, Philadelphia, 1976.

[3] Nicola Marzari, Arash A. Mostofi, Jonathan R. Yates, Ivo Souza, and David Vanderbilt. Maximally localized wannier functions: Theory and applications. *Rev. Mod. Phys.*, 84:1419–1475, Oct 2012.

[4] Daniel Adam Steck. Rubidium 87 d line data. Available online, http://steck.us/alkalidata, April 2018. revision 2.1.5.

[5] Karina Jimenez-Garcia. *Artificial Gauge Fields for Ultracold Neutral Atoms*. PhD thesis, Joint Quantum Institute, National Institute of Standards and Technology, and the University of Maryland, 2012.

[6] K. Jiménez-García, L. J. LeBlanc, R. A. Williams, M. C. Beeler, A. R. Perry, and I. B. Spielman. Peierls substitution in an engineered lattice potential. *Phys. Rev. Lett.*, 108:225303, May 2012.

[7] Daniel Adam Steck. Quantum and atom optics. Available online at http://steck.us/teaching, January 2015. revision 0.12.2.

[8] Lindsey J. LeBlanc. *Exploring many-body physics with ultracold atoms*. PhD thesis, University of Toronto, 2011.

[9] W. Ketterle, D. S. Durfee, and D. M. Stamper-Kurn. Making, probing and understanding Bose-Einstein condensates. In *Bose-Einstein condensation in atomic gases, Proceedings of the International School of Physics 'Enrico Fermi'*, Course CXL, 1999.

[10] K. Aikawa, A. Frisch, M. Mark, S. Baier, R. Grimm, and F. Ferlaino. Reaching fermi degeneracy via universal dipolar scattering. *Phys. Rev. Lett.*, 112:010404, Jan 2014.

[11] M. Lu, N. Q. Burdick, and B. L. Lev. Quantum degenerate dipolar fermi gas. *Phys. Rev. Lett.*, 108:215301, May 2012.

[12] W. Ketterle and M. W. Zwierlein. Making, probing and understanding ultracold Fermi gases. In *Ultracold Fermi Gases, Proceedings of the International School of Physics 'Enrico Fermi', Course CLXIV*, Varenna, 20-30 June 2006.

[13] M. Greiner, C. A. Regal, and D. S. Jin. Emergence of a molecular Bose-Einstein condensate from a Fermi gas. *Nature*, 426(6966):537–540, 2003.

[14] M. W. Zwierlein, C. A. Stan, C. H. Schunck, S. M. F. Raupach, S. Gupta, Z. Hadzibabic, and W. Ketterle. Observation of Bose-Einstein condensation of molecules. *Phys. Rev. Lett.*, 91:250401, 2003.

[15] S. Jochim, M. Bartenstein, A. Altmeyer, G. Hendl, S. Riedl, C. Chin, J. Hecker Denschlag, and R. Grimm. Bose-Einstein condensation of molecules. *Science*, 302(5653):2101–2103, 2003.

[16] M. Bartenstein, A. Altmeyer, S. Riedl, S. Jochim, C. Chin, J. Hecker Denschlag, and R. Grimm. Collective excitations of a degenerate gas at the bec-bcs crossover. *Phys. Rev. Lett.*, 92:203201, 2004.

[17] T. Bourdel, L. Khaykovich, J. Cubizolles, J. Zhang, F. Chevy, M. Teichmann, L. Tarruell, S. J. J. M. F. Kokkelmans, and C. Salomon. Experimental Study of the BEC-BCS Crossover Region in Lithium 6. *Phys. Rev. Lett.*, 93:050401, 2004.

[18] M. W. Zwierlein, C. A. Stan, C. H. Schunck, S. M. F. Raupach, A. J. Kerman, and W. Ketterle. Condensation of pairs of Fermionic atoms near a Feshbach resonance. *Phys. Rev. Lett.*, 92:120403, 2004.

[19] C. A. Regal, M. Greiner, and D. S. Jin. Observation of resonance condensation of fermionic atom pairs. *Phys. Rev. Lett.*, 92(4), 2004.

[20] C. Chin, R. Grimm, P. Julienne, and E. Tiesinga. Feshbach resonances in ultracold gases. *Rev. Mod. Phys.*, 82:1225–1286, 2010.

[21] E. Timmermans, P. Tommasini, M. S. Hussein, and A. Kerman. Feshbach resonances in atomic Bose-Einstein condensates. *Physics Reports-review Section Of Physics Letters*, 315(1-3):199–230, 1999.

[22] E. Tiesinga, B. J. Verhaar, and H. T. C. Stoof. Threshold and resonance phenomena in ultracold ground-state collisions. *Phys. Rev. A*, 47(5, B):4114–4122, 1993.

[23] M. Lysebo and L. Veseth. *Ab initio* calculation of Feshbach resonances in cold atomic collisions: s- and p-wave Feshbach resonances in $^6Li_2$. *Phys. Rev. A*, 79:062704, 2009.

[24] B. Gao. Analytic description of atomic interaction at ultracold temperatures. II. Scattering around a magnetic Feshbach resonance. *Phys. Rev. A*, 84:022706, 2011.

[25] S. Inouye, M. R. Andrews, J. Stenger, H. J. Miesner, D. M. Stamper-Kurn, and W. Ketterle. Observation of Feshbach resonances in a Bose-Einstein condensate. *Nature*, 392(6672):151–154, 1998.

[26] S. L. Cornish, N. R. Claussen, J. L. Roberts, E. A. Cornell, and C. E. Wieman. Stable Rb-85 Bose-Einstein condensates with widely tunable interactions. *Phys. Rev. Lett.*, 85(9):1795–1798, 2000.

[27] C. A. Regal and D. S. Jin. Measurement of positive and negative scattering lengths in a Fermi gas of atoms. *Phys. Rev. Lett.*, 90:230404, 2003.

[28] K. M. O'Hara, S. L. Hemmer, M. E. Gehm, S. R. Granade, and J. E. Thomas. Observation of a strongly interacting degenerate Fermi gas of atoms. *Science*, 298(5601):2179–2182, 2002.

[29] C. Monroe, E. Cornell, C. Sackett, C. Myatt, and C. Wieman. Measurement of Cs-Cs elastic scattering at $T =$30 μK. *Phys. Rev. Lett.*, 70:414–417, 1993.

[30] R. A. Williams, M. C. Beeler, L. J. LeBlanc, K. Jiménez-García, and I. B. Spielman. Raman-induced interactions in a single-component Fermi gas near an s-wave Feshbach resonance. *Phys. Rev. Lett.*, 111:095301, 2013.

[31] Y.-J. Lin, A. R. Perry, R. L. Compton, I. B. Spielman, and J. V. Porto. Rapid production of [87]Rb Bose-Einstein condensates in a combined magnetic and optical potential. *Phys. Rev. A*, 79:063631, 2009.

[32] Thorseten Best. *Interacting Bose-Fermi mixtures in optical lattices*. PhD thesis, Johannes Gutenberg-Universitat, 2010.

[33] B. DeMarco, J. L. Bohn, J. P. Burke, M. Holland, and D. S. Jin. Measurement of p-wave threshold law using evaporatively cooled fermionic atoms. *Phys. Rev. Lett.*, 82:4208–4211, 1999.

[34] S. Wu, Y.-J. Wang, Q. Diot, and M. Prentiss. Splitting matter waves using an optimized standing-wave light-pulse sequence. *Phys. Rev. A*, 71:043602, 2005.

[35] M. Edwards, B. Benton, J. Heward, and C. W. Clark. Momentum-space engineering of gaseous bose-einstein condensates. *Phys. Rev. A*, 82:063613, 2010.

[36] K. v. Klitzing, G. Dorda, and M. Pepper. New method for high-accuracy determination of the fine-structure constant based on quantized hall resistance. *Phys. Rev. Lett.*, 45:494–497, Aug 1980.